

# Finite-amplitude crossflow vortices, secondary instability and transition in the rotating-disk boundary layer

By BENOÎT PIER†

Department of Applied Mathematics and Theoretical Physics, University of Cambridge,  
Centre for Mathematical Sciences, Wilberforce Road, Cambridge, CB3 0WA, UK

(Received 6 December 2002 and in revised form 17 March 2003)

In the three-dimensional boundary layer produced by a rotating disk, the experimentally well-documented sharp transition from laminar to turbulent flow is shown to coincide with secondary absolute instability of the naturally selected primary nonlinear crossflow vortices. Fully saturated primary finite-amplitude waves and the associated nonlinear dispersion relation are first numerically computed using a local parallel flow approximation. Exploiting the slow radial development of the basic flow, the naturally selected primary self-sustained flow structure is then derived by asymptotic analysis. In this state, outward-spiralling nonlinear vortices are initiated at the critical radius where primary absolute instability first occurs. A subsequent secondary stability analysis reveals that as soon as the primary nonlinear waves come into existence they are absolutely unstable with respect to secondary perturbations. Secondary disturbances growing in time at fixed radial locations continuously perturb the primary vortices, thus triggering the direct route to turbulence prevailing in this configuration.

---

## 1. Introduction

The flow due to an infinite disk rotating in otherwise still fluid has served as the archetypal configuration for the study of three-dimensional boundary layers ever since von Kármán (1921) obtained the basic flow as an exact similarity solution of the Navier–Stokes equations. Interest in this flow has been renewed by Lingwood's (1995) discovery that it exhibits a transition from local linear convective to absolute instability at a radius  $R^{ca}$  which closely corresponds to the location of experimentally observed turbulence onset (Theodorsen & Regier 1944; Gregory, Stuart & Walker 1955; Chin & Litt 1972; Fedorov, *et al.* 1976; Kobayashi, Kohama & Takamadate 1980; Malik, Wilkinson & Orszag 1981; Lingwood 1996). The present investigation, inspired by Lingwood's (1995) result, addresses the fully nonlinear régime. The objective is to analyse the naturally selected finite-amplitude state and its secondary stability properties in order to elucidate the process responsible for the sudden transition to turbulence.

The Kármán boundary layer is a rather crude and academic representation of a centrifugal pump, a turbomachinery rotor or even of a computer hard disk. However,

† Present address: Laboratoire de mécanique des fluides et d'acoustique, École centrale, 36 avenue Guy-de-Collongue, 69130 Écully, France.

despite its simplicity, it displays most of the features observed in situations of higher complexity or with more elaborate geometries, e.g. with the fluid at infinity in rigid-body rotation at the same or a different rate (Batchelor 1951; Zandbergen & Dijkstra 1987), the flow between a stationary and a rotating disk enclosed by a cylinder (Jarre, Le Gal & Chauve 1996a; Gauthier, Gondret & Rabaud 1999; Schouveiler, Le Gal & Chauve 2001), and the flow in a rotor–stator annular cavity with radial throughflow (Serre, Crespo del Arco & Bontoux 2001a; Serre *et al.* 2001b). The rotating-disk problem is also closely related to the flow over a backward swept wing (Gregory *et al.* 1955; Cebeci & Stewartson 1980; Bippes, Müller & Wagner 1991; Cebeci *et al.* 1991; Lin & Reed 1993; Malik, Li & Chang 1996; Koch 1996), and it is often claimed that their behaviour is governed by analogous principles. All these types of boundary layers display similar three-dimensional velocity profiles, are subject to inviscid crossflow instabilities and undergo transition to turbulent flow, cf. Reed & Saric (1989). Despite intensive work and recent advances, cf. Schmid & Henningson (2000) and Saric, Reed & White (2003), no full understanding of the turbulent breakdown process has yet been achieved. Identification of the mechanism(s) responsible for transition would improve the prediction methods and lead to new and efficient control strategies, of considerable practical importance e.g. to the aeronautics industry.

However the analogy between a rotating disk and a swept wing is not complete. First, the rotating disk displays self-similar velocity profiles, so that only the study of a single flow instance is required, while the swept-wing boundary layer depends on several control parameters such as sweep angle and chordwise pressure gradient. But the essential difference resides in the azimuthal periodicity of the disk, while the wing lacks any periodic coordinate. Thus perturbations may be naturally recycled in the disk flow, and this property greatly affects its long-time behaviour.

Consider the response to a brief and localized perturbation applied in a region where the boundary layer is unstable, e.g. blowing through a small hole in the disk/wing surface. With time, a wavepacket develops that propagates along the surface while it grows in amplitude and size. The interplay of propagation and growth dictates the long-time behaviour. If the wavepacket is blown away by the basic flow faster than it expands, the flow is said to be *convectively unstable* and, without continuous external input, eventually returns to its unperturbed state. If, by contrast, growth of the wavepacket dominates over advection, the medium is said to be *absolutely unstable* and perturbations grow *in situ* without further external forcing (Briggs 1964; Bers 1983; Huerre & Monkewitz 1990).

In the three-dimensional boundary layer produced by a swept wing, wavepackets may be advected along chordwise and spanwise directions: a genuine absolute instability thus requires the disturbances to maintain themselves in both directions. Investigations of the long-time behaviour of the impulse response in the swept-wing problem (Lingwood 1997b; Ryzhov & Terent'ev 1998; Taylor & Peake 1998) have revealed the possibility of a chordwise absolute instability, but no instance of spanwise absolute instability has so far been found, i.e. perturbations grow in time at a fixed chordwise location while they continue to be advected in the spanwise direction so as to eventually be shed from the wing tip. These results suggest that the persistent fluctuations over aircraft wings are triggered by continuous external disturbances such as roughness elements on the surface or atmospheric turbulence.

The rotating-disk boundary layer contrasts with the above scenario. Due to the exact periodicity in the azimuthal coordinate, a mere radial absolute instability (as theoretically established by Lingwood 1995) is a sufficient condition for disturbance

growth at a fixed location. Indeed, a wavepacket triggered by an initial impulse and amplifying at a constant radial position may, in the early stage of its development, be carried around in the azimuthal direction but, in the long term, it will grow and eventually cover the full circumferential extent of the disk. While many experimental studies (Gregory *et al.* 1955; Kohama 1984; Wilkinson & Malik 1985) have focused on perturbations that are fixed with respect to the disk, and thus certainly generated by roughness elements, the study of the impulse response by Lingwood (1996) has experimentally validated the above scenario of self-sustained disturbances triggered by an initial perturbation and surviving without further external input.

The close relationship between global self-sustained oscillations and local absolute instability has been clarified over the past decade by successively considering one-dimensional model equations and the two-dimensional Navier–Stokes equations, first in a linear approximation and then in a fully nonlinear framework: linear model equations (Chomaz, Huerre & Redekopp 1991; Le Dizès *et al.* 1996), linear Navier–Stokes equations (Monkewitz, Huerre & Chomaz 1993), nonlinear model equations (Couairon & Chomaz 1996, 1997*a,b*, 1999*a,b*; Pier & Huerre 1996; Pier *et al.* 1998; Pier, Huerre & Chomaz 2001), nonlinear Navier–Stokes equations (Pier & Huerre 2001*a*; Pier 2002*b*), for a review see Huerre (2000). In the strictly linear framework, these investigations have shown that absolute instability is only a necessary condition for global instability and, in general, an absolutely unstable region of finite extent is a prerequisite. By contrast, the fully nonlinear governing equations admit self-sustained finite-amplitude solutions as soon as a point of local absolute instability appears and in some extreme cases even without absolute instability at all (Couairon & Chomaz 1997*a*). In the context of the rotating-disk flow, recent numerical (Davies & Carpenter 2003) and theoretical (Peake & Garrett 2003) investigations have shown that this configuration does not exhibit global instability in the linear approximation, even though absolute instability prevails in the semi-infinite region beyond a critical radius. These results suggest that only a nonlinear approach can possibly account for the self-sustained behaviour of the rotating-disk flow.

In situations where finite-amplitude waves develop, either as a naturally selected global mode or by continuous external forcing, the question arises of whether this primary nonlinear state is stable with respect to secondary disturbances. The techniques to carry out local secondary stability analyses are now well-established (Herbert 1988): the most common is to derive a Floquet system of linear differential equations with periodic coefficients after linearization of the governing equations about the primary nonlinear waves. Such an analysis requires first computation of the saturated primary periodic solution, e.g. in terms of a Fourier series, and then use of this as the new basic flow, which usually results in a large Floquet eigensystem. In view of this numerical task, when applied to three-dimensional boundary layers, most early secondary stability analyses (Reed 1987; Fischer & Dallmann 1991; Balachandar, Streett & Malik 1992) used the ‘shape assumption’ by which the nonlinear equilibrium solution is replaced by the linear eigenfunction scaled to a finite amplitude. It is only the recently available computing power that has made possible fully consistent secondary stability analyses (Malik, Li & Chang 1994; Högberg & Henningson 1998; Malik *et al.* 1999; Janke & Balakumar 2000; Koch *et al.* 2000; Koch 2002).

Whether or not the primary saturated wavetrain survives in the long-term is determined by the convective or absolute nature of the secondary instability: only absolutely unstable secondary perturbations are able to resist basic flow advection, to grow at fixed spatial locations and to permanently destroy the underlying primary nonlinear wave. The mathematical foundation of secondary absolute instability

analysis has been firmly laid by Brevdo & Bridges (1996), but so far only a few periodic flows have been found to be absolutely unstable (Brancher & Chomaz 1997; Chomaz, Couairon & Julien 1999).

Huerre (1988) appears to be the first to have shown that secondary absolute instability may occur prior to onset of primary absolute instability. This is particularly relevant in the context of self-sustained oscillations, as demonstrated by Couairon & Chomaz (1999*b*) in a study of the Ginzburg–Landau equation: a primary nonlinear global mode exists whenever primary absolute instability occurs; this global mode is dynamically unstable whenever secondary absolute instability prevails for the selected primary nonlinear wavetrain. In familiar scenarios, primary and secondary absolute instability thresholds are crossed successively when a control parameter is increased. A stable global mode is then observed over a finite parameter range. Recent findings by Le Gal *et al.* (2003) seem to indicate that this scenario applies to the Batchelor flow between a rotating and a stationary disk. However, the order of thresholds may be reversed, and then the primary nonlinear global mode is unstable as soon as it comes into existence. In this latter situation, which is shown in the present paper to apply to the Kármán boundary layer over a single rotating disk, the global instability at the primary threshold leads in a single step to a disordered state.

As discussed above, the boundary layer over a swept wing does not display primary absolute instability and thus does not give rise to self-sustained fluctuations. Nonetheless, transition in that flow could be due to secondary absolute instability of the primary waves produced by roughness elements. In recent studies, Koch *et al.* (2000) and Koch (2002) have computed saturated zero-frequency crossflow vortices and investigated their secondary stability properties ‘in order to examine whether a change from convective to absolute instability is possible in crossflow vortices’. However, despite the remarkable techniques deployed by these authors, no secondary absolute instability has been found and the mechanism of laminar–turbulent breakdown remains to be elucidated in that configuration.

In the rotating-disk flow, azimuthal periodicity appears to facilitate the occurrence of absolute instability thus motivating the present study, a brief account of which has been previously given in Pier (2002*a*). The investigation was carried out in the same spirit as the work by Koch *et al.* (2000) and Koch (2002), and the outline is as follows. The self-similar laminar basic flow is presented in §2 and the governing equations of the problem are given in §3. For the sake of completeness the primary local linear stability characteristics are briefly reviewed in §4 although these results are already well-established (Cebeci & Stewartson 1980; Malik *et al.* 1981; Malik 1986; Bassom & Gajjar 1988; Balakumar & Malik *et al.* 1990; Bassom & Hall 1991; Cebeci *et al.* 1991; Faller 1991; Lin & Reed 1993; Malik *et al.* 1994; Lingwood 1995). The core of the study is then aimed at characterizing and understanding the fully nonlinear régime. Local properties of fully nonlinear waves are computed in §5 as solutions of a local nonlinear dispersion relation. Following the results of Pier *et al.* (2001), the naturally selected spatially extended global solution is derived in §6 by asymptotic matching of these linear and nonlinear wavetrains. Finally, the stability of this self-sustained structure with respect to secondary perturbations is investigated in §7 and the existence of a secondary absolute instability is established.

## 2. Laminar basic flow

The rotating-disk configuration calls for a formulation using cylindrical coordinates. Throughout this investigation an inertial frame of reference is used with  $r$ ,  $\theta$  and  $z$

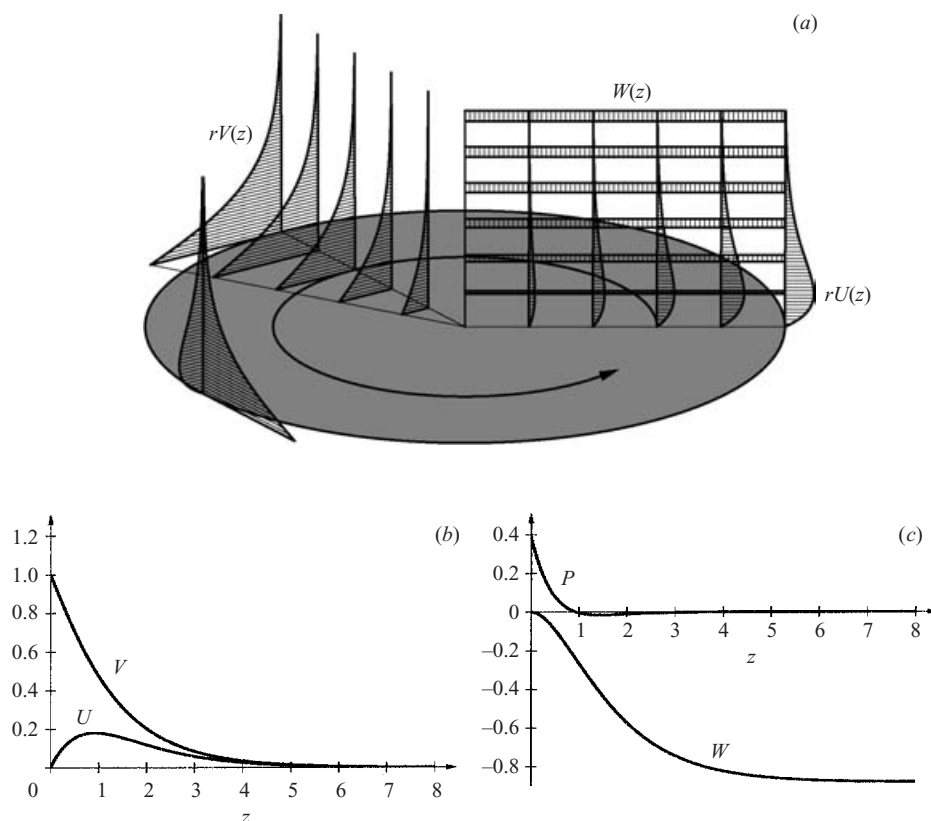


FIGURE 1. Basic flow over a rotating disk. (a) Radial  $rU(z)$  and azimuthal  $rV(z)$  velocity profiles linearly increase with radial distance while the axial flow  $W(z)$  towards the disk surface does not depend on radius. (b, c) Similarity profiles of radial  $U$ , azimuthal  $V$  and axial  $W$  velocity components and pressure  $P$ .

denoting radial, azimuthal and axial coordinates respectively. The fluid in the domain  $z > 0$  is brought into motion by the disk rotating at constant angular frequency about the axis  $r = 0$  normal to the disk surface (figure 1a). The fluid near the disk acquires, by viscous stresses, an azimuthal velocity  $rV(z)$  which linearly increases with radial distance. This circular motion results in centrifugal forces pulling the fluid outwards. The radial outflow  $rU(z)$  induces, by continuity, a weak axial flow component  $W(z)$  towards the disk. This axial flow reaches a constant value far from the disk surface and counteracts diffusion of vorticity away from the disk, thus maintaining a constant boundary layer thickness in the entire system (Batchelor 1967).

The infinite-disk problem lacks a characteristic length scale and thus allows the use of non-dimensional variables based on disk rotation rate, kinematic viscosity and fluid density, so that the flow does not depend on any control parameter. The time-independent axisymmetric basic flow is then given by von Kármán's (1921) exact similarity solution to the Navier–Stokes equations in cylindrical coordinates as

$$\mathbf{U}(r, z) \equiv \begin{pmatrix} rU(z) \\ rV(z) \\ W(z) \end{pmatrix} \quad \text{and} \quad P(z), \quad (2.1)$$

where  $rU$ ,  $rV$  and  $W$  are the non-dimensional radial, azimuthal and axial velocity components respectively and  $P$  is the pressure. Figure 1(b, c) displays the self-similar components  $U(z)$ ,  $V(z)$  and  $W(z)$  that are governed by the set of ordinary differential equations

$$U'' = U^2 - V^2 + U'W, \quad (2.2a)$$

$$V'' = 2UV + V'W, \quad (2.2b)$$

$$W' = -2U, \quad (2.2c)$$

with the boundary conditions

$$U(0) = 0, \quad V(0) = 1, \quad W(0) = 0 \quad \text{and} \quad U(\infty) = 0, \quad V(\infty) = 0. \quad (2.3)$$

With a reference pressure at  $z = +\infty$ , the associated local pressure is obtained as

$$P(z) = W'(z) + (W(\infty)^2 - W(z)^2)/2. \quad (2.4)$$

### 3. Mathematical formulation

After separating the total instantaneous flow fields into basic and perturbation quantities according to

$$\left. \begin{aligned} &U(r, z) + \mathbf{u}(r, \theta, z, t), \\ &P(z) + p(r, \theta, z, t), \end{aligned} \right\} \quad (3.1)$$

the momentum and continuity equations for the perturbation may be written as

$$\frac{\partial \mathbf{u}}{\partial t} + (\mathbf{u} \cdot \nabla) \mathbf{u} + \mathcal{L} \mathbf{u} = -\nabla p + \Delta \mathbf{u}, \quad (3.2a)$$

$$\nabla \cdot \mathbf{u} = 0, \quad (3.2b)$$

with the boundary conditions

$$\begin{aligned} \mathbf{u} &= 0, \quad \partial_z p = \partial_{zz} w \quad \text{at} \quad z = 0, \\ \mathbf{u} &= 0, \quad p = 0 \quad \text{at} \quad z = +\infty, \end{aligned}$$

and the notation

$$\begin{aligned} \mathbf{u} &\equiv \begin{pmatrix} u \\ v \\ w \end{pmatrix}, \quad \nabla p \equiv \begin{pmatrix} \partial_r p \\ (\partial_\theta p)/r \\ \partial_z p \end{pmatrix}, \\ (\mathbf{u} \cdot \nabla) \mathbf{u} &\equiv \left( u \frac{\partial}{\partial r} + \frac{1}{r} v \frac{\partial}{\partial \theta} + w \frac{\partial}{\partial z} \right) \mathbf{u} + \frac{1}{r} \begin{pmatrix} -v^2 \\ uv \\ 0 \end{pmatrix}, \\ \mathcal{L} \mathbf{u} &\equiv \left( rU \frac{\partial}{\partial r} + V \frac{\partial}{\partial \theta} + W \frac{\partial}{\partial z} \right) \mathbf{u} + \begin{pmatrix} rU'w \\ rV'w \\ W'w \end{pmatrix} + \begin{pmatrix} Uu - 2Vv \\ Uv + 2Vu \\ 0 \end{pmatrix}, \\ \Delta \mathbf{u} &\equiv \left( \frac{\partial^2}{\partial r^2} + \frac{1}{r^2} \frac{\partial^2}{\partial \theta^2} + \frac{\partial^2}{\partial z^2} \right) \mathbf{u} + \frac{1}{r} \frac{\partial \mathbf{u}}{\partial r} + \frac{1}{r^2} \begin{pmatrix} -u - 2\partial_\theta v \\ -v + 2\partial_\theta u \\ 0 \end{pmatrix}, \\ \nabla \cdot \mathbf{u} &\equiv \frac{\partial u}{\partial r} + \frac{1}{r} u + \frac{1}{r} \frac{\partial v}{\partial \theta} + \frac{\partial w}{\partial z}. \end{aligned}$$



The boundary layer thickness is constant in the entire system, of order unity in non-dimensional coordinates, while the non-axial velocity components linearly increase with radius. Hence when investigating features far from the disk axis and near a given radial location  $R \gg 1$ , the assumption of slow radial development is appropriate. Local properties for  $r \simeq R$  are then derived by freezing the variable  $r$  which appears in the coefficients of the governing equations above and studying the corresponding three-dimensional flow

$$U(z; R) \equiv \begin{pmatrix} RU(z) \\ RV(z) \\ W(z) \end{pmatrix}. \quad (3.3)$$

This is the parallel-flow assumption: equations (3.2) with the variable  $r$  replaced by the prescribed value of  $R$  are homogenous in both  $\theta$  and  $r$  and will be referred to as the *local governing equations*. Local linear and nonlinear characteristics are derived from these equations; the link between local properties and global behaviour will be re-established in §6. Under the parallel-flow assumption, the value of  $R$  appears as a control parameter rather than a variable in the equations. It determines the magnitude of the basic flow velocity components (3.3) and thus plays the role of an effective local Reynolds number.

#### 4. Primary linear instability properties

Under the parallel-flow assumption both  $r$  and  $\theta$  are homogenous directions; infinitesimally small velocity and pressure disturbances prevailing at a given location  $R$  may thus be written in normal-mode form as

$$\left. \begin{aligned} u(r, \theta, z, t) &= \mathbf{u}^l(z; \alpha, \beta; R) \exp i(\alpha r + \beta \theta - \omega t), \\ p(r, \theta, z, t) &= p^l(z; \alpha, \beta; R) \exp i(\alpha r + \beta \theta - \omega t), \end{aligned} \right\} \quad (4.1)$$

where  $\alpha$  is a complex radial wavenumber,  $\beta$  an integer azimuthal mode number,  $\omega$  a complex angular frequency and  $\mathbf{u}^l$ ,  $p^l$  the associated complex velocity and pressure components. After substitution of (4.1) into the linearized version of the local governing equations (3.2), dropping the  $(\mathbf{u} \cdot \nabla) \mathbf{u}$  term and replacing  $r$  by  $R$  in the coefficients, an eigenvalue problem in the axial direction yields the local linear dispersion relation

$$\omega = \Omega^l(\alpha, \beta; R) \quad (4.2)$$

together with the eigenfunctions  $\mathbf{u}^l(z; \alpha, \beta; R)$  and  $p^l(z; \alpha, \beta; R)$ .

##### 4.1. Numerical solution procedure

The differential eigenproblem in the axial coordinate  $z$  is solved via a Chebyshev collocation method (Canuto, Hussaini & Quarteroni 1988). The collocation points  $-1 \leq \xi_i \equiv -\cos(i\pi/N_z) \leq 1$  for  $0 \leq i \leq N_z$  are mapped onto the semi-infinite domain  $0 \leq z \leq +\infty$  through the transformations

$$z = a_* \frac{1 + \xi'}{1 - \xi'} \quad \text{and} \quad \xi' = b_* \xi + (1 - b_*)(\xi^3 + c_*(1 - \xi^2)). \quad (4.3)$$

The parameters  $a_* > 0$ ,  $0 < b_* \leq 1$  and  $0 \leq c_* \leq 1$  determine the distribution of the collocation points on the  $z$ -axis: with  $c_* = 0$ , half of the points are located in the interval  $0 \leq z \leq a_*$ , while the remaining points are stretched towards  $z = +\infty$  with an algebraically decreasing density; the parameters  $b_*$  and  $c_*$  allow refined

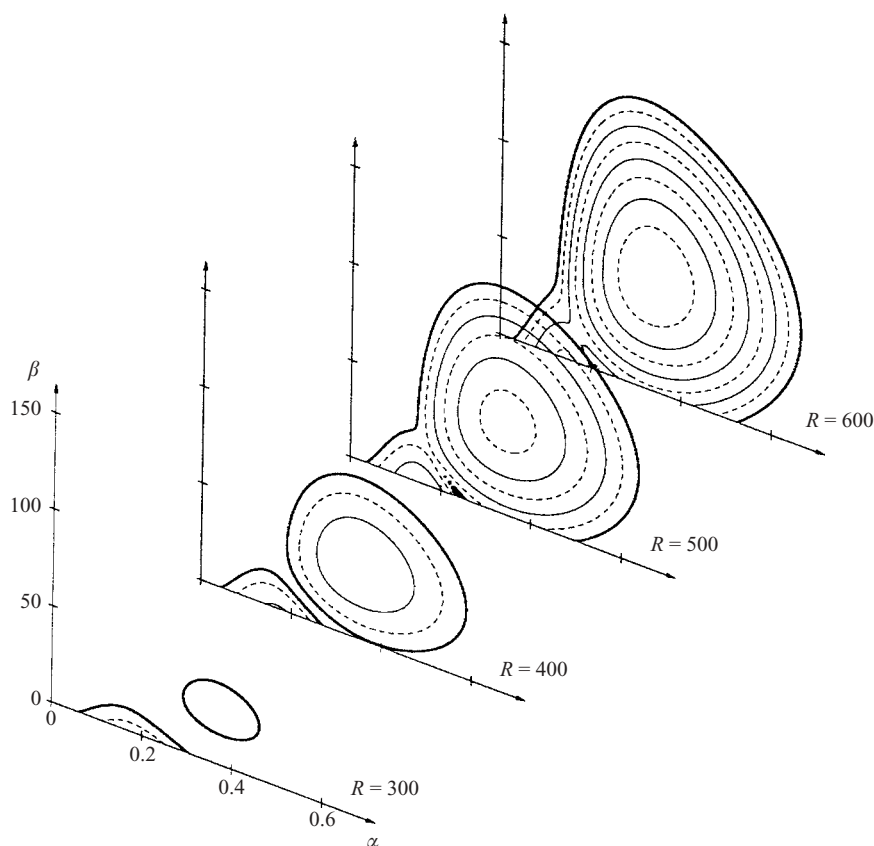


FIGURE 2. Local primary linear dispersion relation. Isocontours of the temporal growth rate  $\Omega_i^l$  in  $(\alpha, \beta)$ -planes for  $R = 300, \dots, 600$ .  $\Omega_i^l = 0$  thick curves,  $\Omega_i^l = 1, 2, 3$  thin solid curves,  $\Omega_i^l = 0.5, 1.5, 2.5, 3.5$  thin dashed curves.

control of the distribution, smaller values of  $b_*$  resulting in a better resolution of the region corresponding to  $\xi = 0$ . A similar mapping has been used by Balachandar *et al.* (1992).

The numerical discretization yields a large number of spurious eigenvalues and eigenfunctions. The physically relevant solutions are identified by inspection of the eigenfunctions, which are required not to vary with increasing resolution. Extensive resolution tests have revealed that remapping the collocation points via (4.3) with  $a_* = 2$ ,  $b_* = 0.6$  and  $c_* = 0.5$  is the most appropriate choice for the various numerical procedures implemented in the present investigation. Unless otherwise stated, these parameters are used throughout the rest of the paper. In general  $N_z = 40$  collocation points are found to very accurately resolve the eigenfunctions. Due to the spectral accuracy of this method, a lower resolution of  $N_z = 30$  still yields quite reliable results and has been used in situations where  $N_z = 40$  would require prohibitively long computational time. Various resolution tests are reported in the Appendix.

#### 4.2. Linear dispersion relation

Temporal growth rates of the local linear dispersion relation are given in figure 2. Two types of modes are identified: the region of main interest is centred around finite values of  $\beta$  and corresponds to an inviscid instability, also known as branch 1, caused



by inflection points in the basic velocity profiles. The maximum growth rate increases with Reynolds number  $R$  and the first inviscid instability occurs for  $R \simeq 284$  at  $\alpha \simeq 0.37$  and  $\beta = 27$ . The unstable modes prevailing at small values of  $\beta$ , also known as branch 2, are due to viscosity and persist at low  $R$ . These latter modes are not relevant to the present investigation and will not be discussed further.

#### 4.3. Local absolute frequency

In the context of self-sustained fluctuations, a crucial feature is the complex absolute frequency  $\omega_0$  defined as the frequency observed at a fixed spatial location in the long-time linear response to an initial localized impulse. For a radially localized impulse with a given azimuthal mode number  $\beta$ , the local absolute frequency  $\omega_0$  and associated absolute wavenumber  $\alpha_0$  are derived from the linear dispersion relation (4.2) by applying the Briggs (1964) and Bers (1983) pinch-point criterion which is associated with a vanishing radial group velocity condition:

$$\omega_0(\beta; R) = \Omega^l(\alpha_0, \beta; R) \quad \text{with} \quad \frac{\partial \Omega^l}{\partial \alpha}(\alpha_0, \beta; R) = 0. \quad (4.4)$$

Isolines of absolute frequency  $\omega_{0,r}$  and growth rate  $\omega_{0,i}$  in the  $(R, \beta)$ -plane are given in figure 3. As already discovered by Lingwood (1995) (see also Lingwood 1997*a*, p. 424 for the corrected values) transition from local convective to absolute instability first occurs at  $R^{ca} \simeq 507.4$  for  $\beta = 68$  (marked by solid dots) with a marginal real absolute frequency of  $\omega_0^{ca} \simeq 50.5$  and  $\alpha_0^{ca} \simeq 0.227 - 0.122i$  (see also § A.1).

Computation of the neutral curve  $\omega_{0,i} = 0$  (thick line in figure 3*b*) shows that each mode number  $\beta \geq 51$  is associated with an absolutely unstable region. The radial extent of the absolutely unstable interval remains finite for all  $\beta$ ; absolute instability has been shown by Peake & Garrett (2003) to prevail for  $3.8 < R/\beta < 38.6$  in the limit  $\beta \rightarrow \infty$ .

### 5. Primary saturated crossflow vortices

Whenever infinitesimally small perturbations are amplified according to the above linear stability results, they eventually reach finite-amplitude levels and are then governed by the complete nonlinear equations. Several experimental studies, e.g. by Kohama (1984), Jarre, Le Gal & Chauve (1996*b*), reveal a pattern of outward-spiralling crossflow vortices before transition to a turbulent régime occurs. These finite-amplitude spiral vortices are periodic in space and time and can be sought as nonlinearly saturated wavetrains evolving in the three-dimensional boundary layer.

Local nonlinearly saturated waves arise naturally from a purely temporal analysis. The initial-value problem of interest is the temporal development of a radially and azimuthally periodic small-amplitude perturbation of the form (4.1), characterized by real values  $\alpha$ , evolving in the three-dimensional flow (3.3) pertaining to a prescribed radial station  $R$ . The initial evolution is dictated by the linear temporal growth rate  $\Omega_i^l(\alpha, \beta; R)$ . Whenever  $\Omega_i^l(\alpha, \beta; R) > 0$ , exponential temporal growth takes place until nonlinear effects come into play. The quadratic nonlinear terms of the Navier–Stokes equations then promote higher spatial harmonics of the form  $\exp in(\alpha r + \beta \theta)$  as well as a mean flow correction. These nonlinearities are stabilizing and lead to saturation at finite amplitude. In the absence of secondary instabilities, a fully nonlinear travelling wave is then reached in the long-time limit with spatial periodicity imposed by the prescribed values of  $\alpha$  and  $\beta$ . The final perturbation velocity and pressure fields

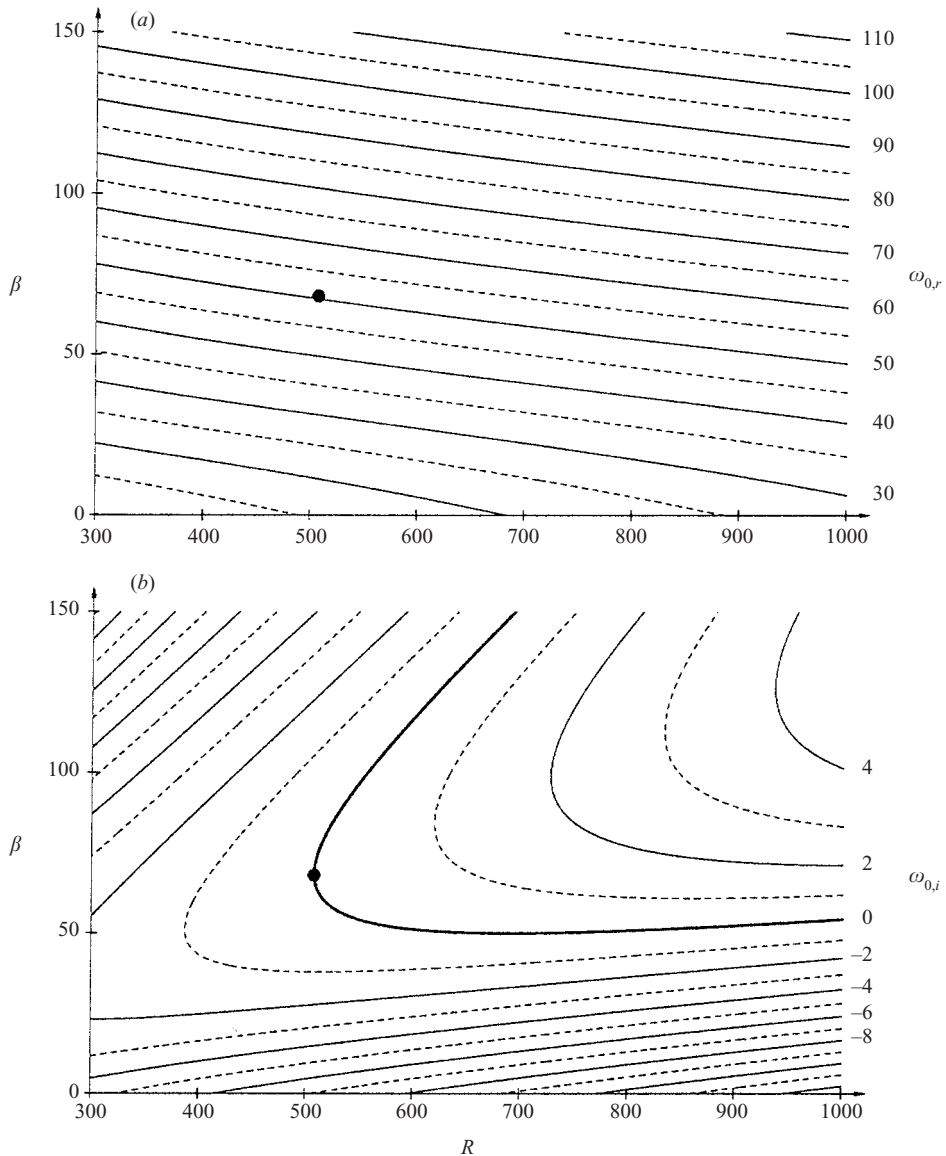


FIGURE 3. Primary local absolute frequency. Isolines of (a)  $\omega_{0,r}$  and (b)  $\omega_{0,i}$  in  $(R, \beta)$ -plane. The solid dot marks the onset of absolute instability at  $R^{ca} \simeq 507$  and  $\beta = 68$  with  $\omega_0^{ca} \simeq 50.5$ .

associated with the travelling saturated crossflow vortices are thus of the form

$$\left. \begin{aligned} \mathbf{u}(r, \theta, z, t) &= \mathbf{u}^{nl}(z, \alpha r + \beta \theta - \omega t; \alpha, \beta; R), \\ p(r, \theta, z, t) &= p^{nl}(z, \alpha r + \beta \theta - \omega t; \alpha, \beta; R), \end{aligned} \right\} \quad (5.1)$$

where the functions  $\mathbf{u}^{nl}$  and  $p^{nl}$  are  $2\pi$ -periodic in their second variable  $\phi \equiv \alpha r + \beta \theta - \omega t$ . The real frequency  $\omega$  of the saturated waves is determined by the local nonlinear dispersion relation

$$\omega = \Omega^{nl}(\alpha, \beta; R), \quad (5.2)$$

while the wave amplitude is conveniently measured by the mean fluctuating energy defined below in (5.5). In the present section the existence of these finite-amplitude travelling waves is studied. Their stability with respect to secondary perturbations is investigated in §7.

Note that instead of using radial wavenumber  $\alpha$  and azimuthal mode number  $\beta$ , it is sometimes appropriate to specify the crossflow vortices by the wave angle  $\varepsilon$  and wave vector modulus  $a$ . These equivalent representations are related by

$$\left. \begin{aligned} \tan \varepsilon &= \beta/R\alpha, & \alpha &= a \cos \varepsilon, \\ a^2 &= \alpha^2 + (\beta/R)^2, & \beta/R &= a \sin \varepsilon. \end{aligned} \right\} \quad (5.3)$$

### 5.1. Numerical solution procedures

The temporal evolution of a spatially periodic perturbation of real radial wavenumber  $\alpha$  and azimuthal mode number  $\beta$  is treated by resorting to the spatial Fourier series

$$\left. \begin{aligned} \mathbf{u}(r, \theta, z, t) &= \sum_n \begin{pmatrix} u_n(z, t) \\ v_n(z, t) \\ w_n(z, t) \end{pmatrix} \exp in(\alpha r + \beta \theta), \\ p(r, \theta, z, t) &= \sum_n p_n(z, t) \exp in(\alpha r + \beta \theta). \end{aligned} \right\} \quad (5.4)$$

Substitution of expansions (5.4) into the local governing equations (3.2) yields an infinite set of coupled differential equations of first order in time. These are truncated at a finite number of harmonics  $|n| \leq N_h$  and the Chebyshev collocation method (4.3) is again used in the axial direction.

Time-integration of the resulting system is performed via a fractional-step method of second-order accuracy in time. At the intermediate time step, the three components of the velocity field are obtained by solving Helmholtz-type problems. A Poisson problem then yields a correction to the pressure required to enforce divergence-free velocity fields. A Crank–Nicholson scheme is used for the viscous terms, the advection terms are obtained at the intermediate time step by extrapolation based on the two previous time steps.

When initializing the temporal integration with the linear eigenmode at small amplitude in a configuration where  $\Omega_i^l(\alpha, \beta; R) > 0$ , the system evolves from an initial exponential growth phase, via a transient régime, to reach a time-periodic state corresponding to fully saturated crossflow vortices travelling without deformation. Measuring the frequency of this wave then yields the nonlinear dispersion relation (5.2), while the fluctuating energy is derived from the Fourier components as

$$E(\alpha, \beta; R) = \int_0^\infty dz \sum_{n>0} (|u_n(z)|^2 + |v_n(z)|^2 + |w_n(z)|^2). \quad (5.5)$$

This time-marching technique fails to converge towards a periodic solution when the primary finite-amplitude vortices are affected by secondary instabilities. In order to capture all primary nonlinear states, whether or not they are unstable with respect to secondary instabilities, a Newton–Raphson search procedure has been implemented that directly solves for the saturated time-periodic waves. In this formulation, the

periodic solution is expanded as

$$\left. \begin{aligned} \mathbf{u}^{nl}(z, \alpha r + \beta \theta - \omega t) &= \sum_n \begin{pmatrix} u_n(z) \\ v_n(z) \\ w_n(z) \end{pmatrix} \exp in(\alpha r + \beta \theta - \omega t), \\ p^{nl}(z, \alpha r + \beta \theta - \omega t) &= \sum_n p_n(z) \exp in(\alpha r + \beta \theta - \omega t), \end{aligned} \right\} \quad (5.6)$$

and substituted into the local governing equations. Truncating at a finite number of harmonics and implementing the collocation method in the  $z$ -direction then results in a large system of nonlinear algebraic equations relating all components of the wave fields and the real parameters  $\alpha$ ,  $\beta$ ,  $\omega$  and  $R$ . To fix the phase of the solution, the normalization condition  $\text{Im } p_1(0) = 0$  is used. A good initial guess for Newton–Raphson iteration is available from the above time-marching procedure using parameter settings that are stable with respect to secondary perturbations. In practice, the lengthy time-marching technique is only used once; the complete set of nonlinear waves is thereafter obtained by the much faster iteration procedure, continuously varying the parameters.

In general,  $\beta$  and  $R$  are kept at fixed values, and the nonlinear dispersion relation (5.2) is then obtained by following temporal branches, i.e. continuously varying  $\alpha$  and solving for the wave fields and frequency  $\omega$ . A further difficulty arises due to the existence of critical values of  $\alpha$  where the Jacobian used in the Newton–Raphson iteration procedure becomes singular. These singularities are associated with turning points and the fact that (5.2) is not single-valued in a small region of the parameter space. In order to follow solution branches past these turning points, the usual continuation in  $\alpha$  must be replaced by an arclength continuation (Keller 1977). For the present purpose it is convenient to consider both  $\alpha$  and  $\omega$  as unknowns and to complement the governing system by a parameterizing equation

$$\Pi(\alpha, \omega; s) = 0, \quad (5.7)$$

where  $s$  denotes an arclength coordinate in the  $(\alpha, \omega)$ -plane. Following of the entire solution branch is then achieved using a simplified version of the pseudo-arclength parameterization of Keller (1977),

$$\Pi \equiv (1 - \mu)[\alpha(s) - \alpha(s_0)] \frac{d\alpha}{ds}(s_0) + \mu[\omega(s) - \omega(s_0)] \frac{d\omega}{ds}(s_0) - (s - s_0), \quad (5.8)$$

where  $s_0$  denotes the arclength coordinate at the previously computed point and the constant  $0 \leq \mu \leq 1$  controls the relative importance given to variations in  $\alpha$  or  $\omega$ . Note that the limiting values  $\mu = 0$  and  $\mu = 1$  yield the nonlinear temporal and spatial branches, respectively parameterized by  $\alpha$  and  $\omega$ .

### 5.2. Nonlinear wave near onset of primary absolute instability

As shown below in § 6, the transition location  $R^{ca} = 507.4$  from convective to absolute instability is of particular importance for the self-sustained behaviour of the rotating-disk flow. Figure 4 illustrates the structure of the nonlinear saturated waves prevailing near onset of absolute instability, at  $R = 510$  and  $\beta = 68$ . The waves shown are  $2\pi$ -periodic in the phase variable  $\phi \equiv \alpha r + \beta \theta - \omega t$  and propagate according to a frequency of  $\omega = 50.5$  and a radial wavenumber of  $\alpha = 0.35$  (see also § A.2). A systematic study of the nonlinear dispersion relation (5.2) is postponed to the next subsection.

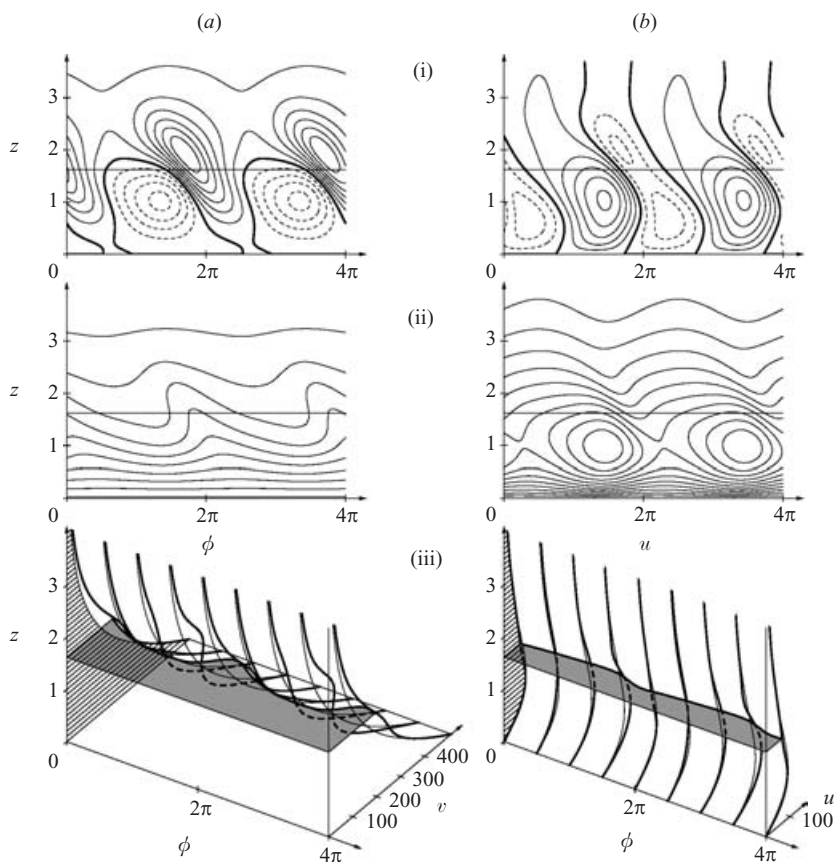


FIGURE 4. Structure of nonlinear saturated wave at  $R = 510$ ,  $\beta = 68$ ,  $\alpha = 0.35$  and  $\omega = 50.5$ . (a) Azimuthal and (b) radial velocity components. (i) Isolines of perturbation velocity fields over two wavelengths (azimuthal levels  $-40, \dots, -10$  dashed, 0 thick,  $10, \dots, 60$  thin; radial levels  $-10, -5$  dashed, 0 thick,  $5, \dots, 25$  thin). (ii) Isolines of total velocity fields (azimuthal levels  $50, 100, \dots, 500$ ; radial levels  $10, 20, \dots, 110$ ). (iii) Comparison of basic (thin lines) and total (thick lines) velocity profiles.

Figure 4(i)(a, b) displays snapshots of the perturbation azimuthal  $v$ - and radial  $u$ -velocity contours over two wavelengths in the  $(z, \phi)$ -plane. The corresponding total components  $RV(z) + v(z, \phi)$  and  $RU(z) + u(z, \phi)$  are shown in figure 4(ii)(a, b). Figure 4(iii)(a, b) compares the total velocity profiles at four different phases  $\phi = 0, \pi/2, \pi$  and  $3\pi/2$  (thick lines) with the basic flow (thin lines). Also shown are cuts of the total velocity fields at  $z = 1.6$  (grey regions). These profiles display several inflection points in both velocity components, most clearly at  $\phi = 3\pi/2$ . It is thus very likely that these saturated crossflow vortices will be unstable with respect to secondary perturbations, as shown in § 7.

### 5.3. Nonlinear dispersion relation and fluctuating energy

The fluctuating energy and nonlinear frequency of waves corresponding to the critical azimuthal wavenumber  $\beta = 68$  are given in figure 5. The energy  $E$ , as defined by (5.5), of the nonlinear solution branches is shown in (a) together with isolines of the positive linear growth rates  $\Omega_i^l$ . As can be seen, the nonlinear amplitude vanishes on

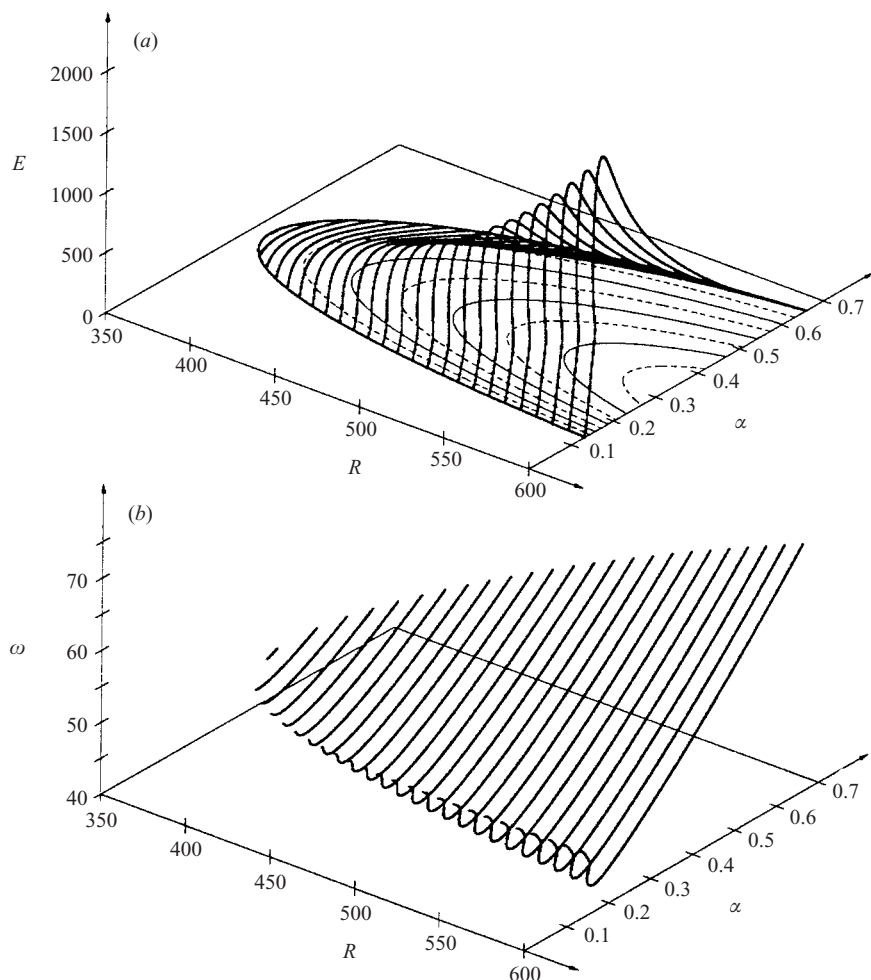


FIGURE 5. Local nonlinear waves in the  $(R, \alpha)$ -plane for a fixed  $\beta = 68$ . (a) Fluctuating energy curves and (b) nonlinear frequency. Also shown in (a) are isolines of linear temporal growth rate (levels 0 thick, 1, 2, 3 thin solid, 0.5, 1.5, 2.5, 3.5 thin dashed).

the neutral curve where  $\Omega_i^l = 0$  while nonlinear waves with largest amplitude occur near the lower end of the  $\alpha$ -wavenumber range and do not coincide with the highest linear growth rates. The frequency curves corresponding to the nonlinear dispersion relation (5.2) are given in figure 5(b). It is towards the lower marginal curve, where the energy sharply drops, that turning points in the dispersion relation occur. These turning points are related to the proximity in parameter space of viscous instability modes; however, since they are not essential in the present investigation no further details will be given here. A similar feature has been found by Koch *et al.* (2000) in the swept-plate boundary layer (see their figure 6).

Saturated waves have been systematically computed for radial locations up to  $R = 600$ . The structure of the nonlinear dispersion relation  $\Omega^{nl}(\alpha, \beta; R)$  is illustrated in figure 6 by cuts of the three-dimensional parameter space along planes of constant azimuthal mode number.

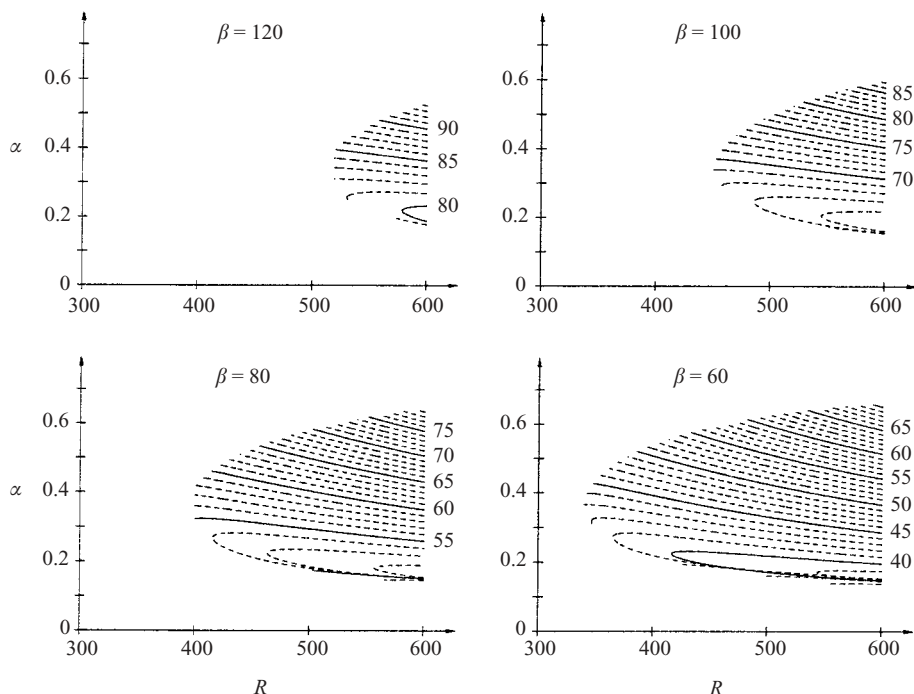


FIGURE 6. Nonlinear dispersion relation  $\Omega^{nl}(\alpha, \beta; R)$ . Isofrequency lines in the  $(R, \alpha)$ -plane for  $\beta = 120, 100, 80$  and  $60$ .

## 6. Self-sustained spatially extended structure

Having obtained the local linear and nonlinear waves in the boundary layer at each radial location in the previous sections, a global solution developing over an extended radial interval may be sought in the form of wavetrains that are slowly modulated in the radial direction. This approach is set on firm theoretical ground using WKBJ asymptotic techniques (Bender & Orszag 1978). Such a line of thought has previously been fully implemented for one-dimensional model equations and the two-dimensional Navier–Stokes equations. The generalization of this formalism to the present three-dimensional case is obtained with no more than algebraic difficulty. Only an outline of the method will be given here.

In the rotating-disk flow, the region of particular interest is the neighbourhood of  $R^{ca} \simeq 507.4$  where onset of absolute instability first occurs. This characteristic radius is large compared to the boundary layer thickness, hence fulfilling the assumption of weak radial development, or equivalently of large Reynolds number since the radius acts as an effective local Reynolds number. It is thus legitimate to use

$$\epsilon \equiv \frac{1}{R^{ca}} \ll 1 \quad (6.1)$$

as small parameter in the asymptotic formulation and to introduce the slow radial coordinate

$$\bar{R} = \epsilon r. \quad (6.2)$$

In this multiple-scales approach, the fast  $r$ -scale accounts for the oscillatory behaviour of the spatially extended wavetrain, while its envelope and local structure are slowly modulated on the  $\bar{R}$ -scale so as to adjust to the variations of the underlying basic



flow. This suggests the following change of variables:

$$\left. \begin{aligned} \mathbf{u}(r, \theta, z, t) &= \mathbf{u}(z, \phi; \bar{R}), \\ p(r, \theta, z, t) &= p(z, \phi; \bar{R}), \end{aligned} \right\} \quad (6.3)$$

with  $2\pi$ -periodicity in the fast phase function  $\phi(r, \theta, t)$  whereas the  $\bar{R}$ -dependence accounts for the slow radial evolution. Local radial wavenumber, azimuthal mode number and frequency are respectively defined as

$$\alpha = \frac{\partial \phi}{\partial r}, \quad \beta = \frac{\partial \phi}{\partial \theta}, \quad \omega = -\frac{\partial \phi}{\partial t}. \quad (6.4)$$

For a global solution displaying no singularities, both the frequency and azimuthal mode number remain constant in the entire system. Indeed, any spatial variation of either of these two quantities necessarily introduces dislocations. A smooth global solution (6.3) is thus made up of waves that all have same global frequency  $\omega_g$  and azimuthal mode number  $\beta_g$ . The fast phase is then of the form

$$\phi = \left( \frac{1}{R^{ca}} \int^{\bar{R}} \alpha(\bar{\rho}) d\bar{\rho} \right) + \beta_g \theta - \omega_g t, \quad (6.5)$$

where  $\alpha(\bar{R})$  is an as yet undetermined slowly varying local radial wavenumber. Next the wave fields and the derivative operators are expanded in powers of  $\epsilon$  as

$$\left. \begin{aligned} \mathbf{u}(z, \phi; \bar{R}) &= \mathbf{u}_0 + \epsilon \mathbf{u}_1 + \epsilon^2 \mathbf{u}_2 + \dots, \\ p(z, \phi; \bar{R}) &= p_0 + \epsilon p_1 + \epsilon^2 p_2 + \dots, \end{aligned} \right\} \quad (6.6)$$

and

$$\frac{\partial}{\partial r} = \alpha(\bar{R}) \frac{\partial}{\partial \phi} + \epsilon \frac{\partial}{\partial \bar{R}}, \quad \frac{\partial}{\partial \theta} = \beta_g \frac{\partial}{\partial \phi}, \quad \frac{\partial}{\partial t} = -\omega_g \frac{\partial}{\partial \phi}, \quad (6.7)$$

and substituted into the governing equations (3.2). At leading order in the expansion parameter  $\epsilon$ , the derivative  $\partial/\partial \bar{R}$  may be neglected and the slow coordinate  $\bar{R}$  acts solely as an external control parameter. For each value of  $\bar{R}$ , the global solution (6.3) then obeys, to leading order, the local governing equations and follows, among all possible waves, the one that matches the overall frequency  $\omega_g$  and mode number  $\beta_g$ . Note that in the previous sections, local properties have been derived with the local Reynolds number  $R$  as control parameter. When carrying out the present asymptotic analysis, however, it is more appropriate to rescale this parameter as  $\bar{R} = \epsilon R$  and to consider that the local properties depend on  $\bar{R}$  instead.

Two different situations arise depending on the magnitude of the global solution (6.3): in small-amplitude regions the global structure is described by the linearized equations while the fully nonlinear equations prevail in regions of finite amplitude.

Small-amplitude regions are governed by the local linear equations and the corresponding dispersion relation (4.2). The radial wavenumber  $\alpha(\bar{R})$  in the rapidly varying phase (6.5) is then complex, accounting for both the wavelength and decay rate in the radial direction, and obtained by solving the linear dispersion relation (4.2) with prescribed  $\beta_g$  and  $\omega_g$ . When solving (4.2) for the wavenumber  $\alpha$ , two complex spatial branches  $\alpha^{\pm}(\bar{R}; \omega_g, \beta_g)$  are obtained. The separation of the spatial branches into  $+$  and  $-$  branches is determined, according to classical arguments (Briggs 1964; Bers 1983), by whether they correspond to a downstream or upstream spatial response to localized harmonic forcing. As discussed below, in the present configuration the

relevant spatial branch in the central linear region is always the  $\alpha^{l-}$  branch. The global solution (6.3), (6.5) then locally follows the wave indexed by  $\alpha^{l-}(\bar{R})$ ,  $\beta_g$  and  $\bar{R}$  within the family (4.1) of linear eigenfunctions.

In contrast, the finite-amplitude régime is governed by the local nonlinear equations and the corresponding dispersion relation (5.2). Solving (5.2) with prescribed  $\beta_g$  and  $\omega_g$  then yields the corresponding real wavenumber branch  $\alpha^{nl}(\bar{R})$ . These nonlinear spatial branches correspond to the isofrequency lines represented in figure 6. This figure also shows that a single nonlinear spatial branch is generally obtained; it is only for lower frequencies than those of interest here that two  $\alpha^{nl}$ -branches coexist. In nonlinear regions, the global solution then locally follows the wavetrains associated with  $\alpha^{nl}(\bar{R})$ ,  $\beta_g$  and  $\bar{R}$  within the family (5.1) of saturated crossflow vortices.

It remains to determine which global frequency  $\omega_g$  and mode number  $\beta_g$  are naturally selected in the rotating-disk flow.

As demonstrated in earlier investigations (Pier *et al.* (2001), spatially developing systems display a nonlinear self-sustained state whenever a region of absolute instability is present. These finite-amplitude solutions (also called ‘elephant’ global modes (Pier & Huerre 2001*b*)) are characterized by a stationary front located at the upstream transition from local convective to absolute instability. The selection mechanism is the following: in the absolutely unstable region amplified perturbations develop and their envelope advances upstream against the basic flow. At the location of neutral absolute instability a balance between upstream perturbation growth and downstream advection is reached and perturbations pile up at that location. Nonlinearities lead to saturation of the fluctuating amplitude and a stationary front is formed. This front generates a downstream-propagating fully nonlinear wavetrain and an upstream exponentially decaying tail. It thus connects linear and nonlinear regions, acts as a source and effectively tunes the entire system to its frequency. The stationary front obeys the Dee & Langer (1983) marginal stability criterion, hence the global frequency of these modes equals the real absolute frequency prevailing at the front location.

In the present configuration, the transition radius from convective to absolute instability depends on the azimuthal mode number  $\beta$  (see the neutral curve in figure 3*b*). Each  $\beta \geq 51$  is associated with an absolutely unstable region and thus gives rise, in principle, to a self-sustained global structure displaying a front at the corresponding marginal radius. However, it is for  $\beta = 68$  that absolute instability first occurs, at  $R^{ca} \simeq 507.4$ , and hence that perturbations are able to propagate inwards closest to the disk centre. Global modes with  $\beta \neq 68$  would reach finite amplitude levels further outwards and are thus dominated by the solution with  $\beta = 68$ .

Assuming for now that there are no secondary instabilities, the expected self-sustained behaviour is thus a time-harmonic solution with frequency  $\omega_g = \omega_0^{ca} \simeq 50.5$  and azimuthal mode number  $\beta_g = 68$ . Onset of nonlinearity coincides with onset of absolute instability and is triggered by a front at  $R^{ca}$ . The spatial structure is the following (figure 7): nonlinear outward-spiralling vortices of frequency  $\omega_g$  and mode number  $\beta_g$  are initiated at  $R^{ca}$  and prevail in the outer region. They are governed by the local nonlinear dispersion relation (5.2) and follow the associated real spatial wavenumber branch  $\alpha^{nl}$  (figure 7*b*). The inner region  $r < R^{ca}$  is covered by the front tail. Since this tail is caused by the front at  $R^{ca}$ , it decays exponentially towards the disk centre according to the complex radial wavenumber  $\alpha^{l-}$  derived from the local linear dispersion relation (4.2). Note that the front at  $R^{ca}$  is associated with a jump in wavenumber from the complex  $\alpha^{l-}$  to the real  $\alpha^{nl}$ . However, the fundamental assumption of slowly varying radial change is not violated: this jump merely reflects

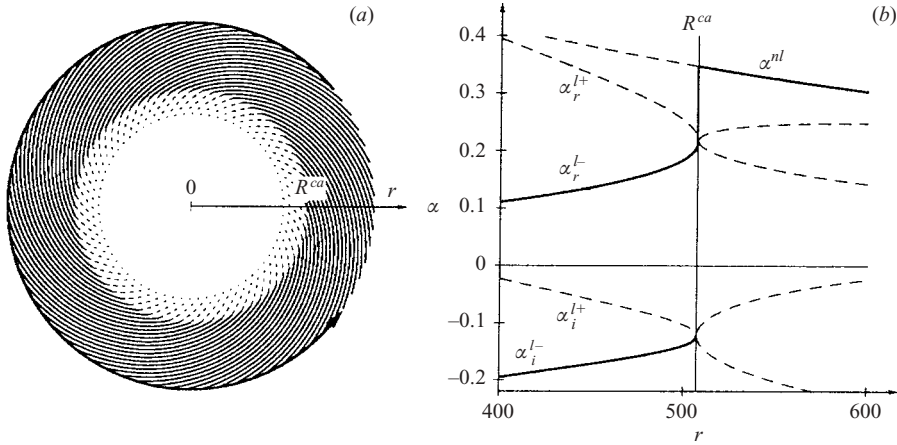


FIGURE 7. Spatial structure of self-sustained nonlinear global solution of frequency  $\omega_0^{ca} \simeq 50.5$  and azimuthal modenumbers  $\beta = 68$ . (a) Sketch of outward-spiralling nonlinear vortices triggered at  $R^{ca} \simeq 507.4$ ; exponentially decaying tail covers the inner region. (b) Corresponding numerically computed spatial branches obtained by solving the linear (two complex branches  $\alpha^{l\pm}$ ) and the nonlinear (real branch  $\alpha^{nl}$ ) dispersion relation. Pinching of the linear branches occurs for the absolute wavenumber  $\alpha_0 = 0.227 - 0.122i$  at  $R^{ca}$ . Radial wavenumber of the global solution follows the path indicated by the thick line: the linear  $\alpha^{l-}$  branch prevails in the central region; the front at  $R^{ca}$  is associated with a jump in wavenumber; the nonlinear  $\alpha^{nl}$  branch prevails in the outer region.

the existence of an inner layer (of size  $\mathcal{O}(\epsilon^{2/3})$  see Pier *et al.* 2001) in the complete asymptotic analysis.

The WKB procedure outlined above guarantees the existence of a global time-harmonic solution but does not tell us whether or not it is stable with respect to secondary perturbations. The experimental observation of a rapid transition to turbulence near  $R^{ca}$  suggests that it is not. The aim of the remainder of this paper is to understand this transition and therefore analyses in detail the secondary stability of the saturated waves that make up the global solution near  $R^{ca}$ .

## 7. Secondary stability analysis

When investigating the stability of primary saturated vortices of wavenumbers  $\alpha$  and  $\beta$  and frequency  $\omega$  at a radial station  $R$  with respect to secondary perturbations, the total flow fields are decomposed as

$$\left. \begin{aligned} &U(z; R) + \mathbf{u}^{nl}(z, \alpha r + \beta \theta - \omega t; \alpha, \beta; R) + \hat{\mathbf{u}}(r, \theta, z, t), \\ &P(z) + p^{nl}(z, \alpha r + \beta \theta - \omega t; \alpha, \beta; R) + \hat{p}(r, \theta, z, t), \end{aligned} \right\} \quad (7.1)$$

where  $U + \mathbf{u}^{nl}$ ,  $P + p^{nl}$  represent the new basic flow solution which is perturbed by  $\hat{\mathbf{u}}$ ,  $\hat{p}$ .

Linear secondary stability of the primary periodic crossflow vortices is governed by Floquet theory (Herbert 1988) and infinitesimally small secondary velocity and pressure disturbances can be written in normal-mode form as

$$\left. \begin{aligned} \hat{\mathbf{u}}(r, \theta, z, t) &= \hat{\mathbf{u}}^l(z, \alpha r + \beta \theta - \omega t; \hat{\alpha}, \hat{\beta}; \alpha, \beta; R) \exp i(\hat{\alpha} r + \hat{\beta} \theta - \hat{\omega} t), \\ \hat{p}(r, \theta, z, t) &= \hat{p}^l(z, \alpha r + \beta \theta - \omega t; \hat{\alpha}, \hat{\beta}; \alpha, \beta; R) \exp i(\hat{\alpha} r + \hat{\beta} \theta - \hat{\omega} t), \end{aligned} \right\} \quad (7.2)$$

where  $\hat{\alpha}$  is the secondary complex radial wavenumber,  $\hat{\beta}$  is the secondary integer azimuthal mode number and  $\hat{\omega}$  is the corresponding complex frequency; the eigenfunctions  $\hat{\mathbf{u}}^l$  and  $\hat{\mathbf{p}}^l$  have the same periodicity as the primary wave, i.e. are  $2\pi$ -periodic in the real phase variable  $\phi \equiv \alpha r + \beta \theta - \omega t$ . Two-dimensional eigenproblems in the variables  $z$  and  $\phi$  are then obtained after substitution of (7.1) with (7.2) into the local governing equations and linearization about the new basic flow. For each primary nonlinear wave characterized by the real parameters  $\alpha$ ,  $\beta$  and  $R$  and for each choice of  $\hat{\alpha}$  and  $\hat{\beta}$ , the solution of the corresponding eigenproblem yields the secondary complex frequency

$$\hat{\omega} = \hat{\mathcal{S}}^l(\hat{\alpha}, \hat{\beta}; \alpha, \beta; R) \quad (7.3)$$

together with the associated eigenfunctions  $\hat{\mathbf{u}}^l$  and  $\hat{\mathbf{p}}^l$ . Note that the eigenproblem admits many modes, but in general only the most unstable are physically relevant.

### 7.1. Numerical solution procedure

The linear local governing equations for the small-amplitude secondary perturbations (7.2) are formally similar to the linearized version of (3.2)

$$\frac{\partial \hat{\mathbf{u}}}{\partial t} + \hat{\mathcal{L}} \hat{\mathbf{u}} = -\nabla \hat{\mathbf{p}} + \Delta \hat{\mathbf{u}}, \quad (7.4a)$$

$$\nabla \cdot \hat{\mathbf{u}} = 0, \quad (7.4b)$$

except that advection occurs by the primary vortices (5.1) as well as by the laminar base flow (3.3) so that now

$$\begin{aligned} \hat{\mathcal{L}} \hat{\mathbf{u}} \equiv & \left( (RU + u^{nl}) \frac{\partial}{\partial r} + \left( V + \frac{1}{R} v^{nl} \right) \frac{\partial}{\partial \theta} + (W + w^{nl}) \frac{\partial}{\partial z} \right) \hat{\mathbf{u}} \\ & + \begin{pmatrix} rU' \hat{w} \\ rV' \hat{w} \\ W' \hat{w} \end{pmatrix} + \left( \hat{\mathbf{u}} \frac{\partial}{\partial r} + \frac{1}{R} \hat{v} \frac{\partial}{\partial \theta} + \hat{w} \frac{\partial}{\partial z} \right) \mathbf{u}^{nl} \\ & + \begin{pmatrix} U \hat{\mathbf{u}} - 2V \hat{v} \\ U \hat{v} + 2V \hat{\mathbf{u}} \\ 0 \end{pmatrix} + \frac{1}{R} \begin{pmatrix} -2v^{nl} \hat{v} \\ u^{nl} \hat{v} + v^{nl} \hat{\mathbf{u}} \\ 0 \end{pmatrix}. \end{aligned}$$

Upon substituting the previously obtained Fourier expansion (5.6) for the primary solution and expanding the secondary eigenfunctions (7.2) in a similar fashion as

$$\left. \begin{aligned} \hat{\mathbf{u}}^l(z, \alpha r + \beta \theta - \omega t) &= \sum_n \begin{pmatrix} \hat{u}_n(z) \\ \hat{v}_n(z) \\ \hat{w}_n(z) \end{pmatrix} \exp in(\alpha r + \beta \theta - \omega t), \\ \hat{\mathbf{p}}^l(z, \alpha r + \beta \theta - \omega t) &= \sum_n \hat{p}_n(z) \exp in(\alpha r + \beta \theta - \omega t), \end{aligned} \right\} \quad (7.5)$$

the local governing equations (7.4) transform into an eigenproblem where the infinite set of eigenfunctions  $\hat{u}_n$ ,  $\hat{v}_n$  and  $\hat{w}_n$  are linearly coupled via the harmonics  $u_n$ ,  $v_n$  and  $w_n$  of the primary wave (5.6). After truncating primary and secondary Fourier expansions at  $|n| \leq N_h$  and  $|n| \leq \hat{N}_h$  respectively and using the Chebyshev collocation method in the  $z$ -direction, a large algebraic eigensystem is obtained, the solution of which yields the secondary dispersion relation (7.3) and the associated eigenfunctions. As for the primary linear stability analysis, the physically relevant modes are identified by monitoring the structure of the eigenfunctions while varying the resolution.

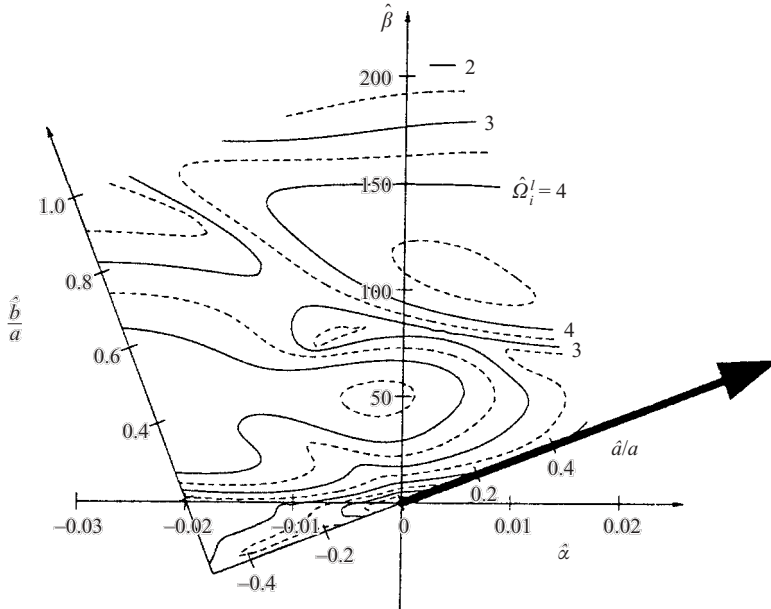


FIGURE 8. Secondary temporal growth rate  $\hat{\Omega}_i^l$  of saturated crossflow vortices prevailing for  $R = 510$ ,  $\beta = 68$ ,  $\alpha = 0.35$  and  $\omega = 50.5$  (levels 1, 2, 3, 4 solid; 0.5, 1.5, 2.5, 3.5, 4.5 dashed). Isoline pattern is invariant under translation of the primary wavevector, indicated by the thick arrow.

### 7.2. Secondary temporal analysis

In a temporal analysis, the radial wavenumber  $\hat{\alpha}$  of the secondary perturbation is prescribed and real, while the frequency  $\hat{\omega}$  as obtained from dispersion relation (7.3) is complex.

Figure 8 shows the secondary temporal growth rate  $\hat{\Omega}_i^l$  in the real  $(\hat{\alpha}, \hat{\beta})$ -plane for the saturated crossflow vortices prevailing near onset of primary absolute instability and analysed in § 5.2. Such results are usually presented by resorting to wave-oriented coordinates, i.e. expressing  $\hat{\alpha}$  and  $\hat{\beta}$  in terms of the wave angle  $\varepsilon$  (5.3) of the primary nonlinear vortices as

$$\left. \begin{aligned} \hat{\alpha} &= \hat{a} \cos \varepsilon - \hat{b} \sin \varepsilon, \\ \hat{\beta}/R &= \hat{a} \sin \varepsilon + \hat{b} \cos \varepsilon, \end{aligned} \right\} \quad (7.6)$$

and prescribing  $\hat{a}$  and  $\hat{b}$  instead of  $\hat{\alpha}$  and  $\hat{\beta}$ . With  $a = \sqrt{\alpha^2 + (\beta/R)^2}$  denoting the primary wavevector modulus, the ratio  $\hat{a}/a$  is the detuning of the primary wavenumber, and  $\hat{b}$  is the secondary wavenumber in the direction of the primary vortex axis. By periodicity of the primary waves it is sufficient to consider the range  $-a/2 \leq \hat{a} \leq a/2$ . Here the parameters of the primary wave are  $R = 510$ ,  $\beta = 68$ ,  $\alpha = 0.35$  and  $\omega = 50.5$  which correspond to  $\varepsilon = 0.368$  and  $a = 0.371$ , and figure 8 shows the highest temporal growth rate of all unstable modes.

From these results it is found that the crossflow vortices under consideration are unstable to secondary perturbations for any  $\hat{a}$  at small and order-unity values of  $\hat{b}$ . It is only at much higher values of  $\hat{b}$  that secondary perturbations are found to decay, since the maximum growth rate decreases with  $\hat{b}$ .

### 7.3. Secondary absolute instability and transition

Whether or not the primary finite-amplitude waves are permanently affected by secondary disturbances depends on the absolute or convective nature of the secondary instability. Indeed, for convectively unstable secondary instabilities, an external impulse may only trigger a transient perturbation that is eventually carried away radially outwards. Without external noise and for a perfectly smooth rotating disk, transition can only occur because of secondary absolute instability of the naturally selected primary crossflow vortices.

In contrast to the previous purely temporal analysis, the use of vortex-oriented coordinates is not appropriate for a full spatio-temporal analysis where the radial wavenumber  $\hat{\alpha}$  needs to be considered complex while the mode number  $\hat{\beta}$  remains integer.

Following Brevdo & Bridges (1996), the secondary absolute frequency  $\hat{\omega}_0$  and absolute radial wavenumber  $\hat{\alpha}_0$  for periodic wave solutions are obtained by a ‘pinching condition’ in the complex  $\hat{\alpha}$ -plane which is formally analogous to that of Briggs (1964) and Bers (1983) established for spatially homogenous systems. This criterion is equivalent to a condition of vanishing radial group velocity,

$$\hat{\omega}_0(\hat{\beta}; \alpha, \beta; R) = \hat{\Omega}^l(\hat{\alpha}_0, \hat{\beta}; \alpha, \beta; R) \quad \text{where} \quad \frac{\partial \hat{\Omega}^l}{\partial \hat{\alpha}}(\hat{\alpha}_0, \hat{\beta}; \alpha, \beta; R) = 0, \quad (7.7)$$

with the additional requirement that the two spatial  $\hat{\alpha}$ -branches colliding at the branch-point singularity  $\hat{\alpha}_0$  originate from distinct half  $\hat{\alpha}$ -planes for sufficiently large and positive values of  $\hat{\omega}_i$ .

Pinch points are readily identified by the ‘cusp map’ method (Kupfer, Bers & Ram 1987), i.e. by monitoring how the dispersion relation (7.3) maps the complex  $\hat{\alpha}$ -plane onto the complex  $\hat{\omega}$ -plane. This process is illustrated in figure 9 for the primary nonlinear wave obtained with  $R = 510$ ,  $\alpha = 0.35$ ,  $\beta = 68$  and  $\omega = 50.5$ ; the secondary azimuthal mode number is fixed at  $\hat{\beta} = 20$ . To start with, dispersion relation (7.3) is computed on a coarse rectangular grid in the complex wavenumber plane (part of which is shown by solid dots in figure 9a) to yield an outline of the mapping in the frequency plane (figure 9b) and the approximate location of a potential pinch point. Zooming in and recomputing the dispersion relation for a refined rectangular grid in the wavenumber plane reveals the characteristic cusp in the frequency plane (magnified portion of figure 9b). The corresponding values of the absolute frequency and wavenumber

$$\hat{\omega}_0 = 8.52 + 1.16i \quad \text{and} \quad \hat{\alpha}_0 = -0.0012 - 0.0369i \quad (7.8)$$

are then found by solving  $\partial \hat{\Omega}^l / \partial \hat{\alpha} = 0$  (see also §A.3). In order to ascertain that this singularity of  $\hat{\Omega}^l$  corresponds to a genuine pinch point, the two spatial branches  $\hat{\alpha}^+(\hat{\omega})$  and  $\hat{\alpha}^-(\hat{\omega})$  are computed for  $\hat{\omega} = \hat{\omega}_{0,r} + \hat{\omega}_i$  with  $\hat{\omega}_i \downarrow \hat{\omega}_{0,i}$  (thick curve in figure 9b). The curves labelled  $\hat{\alpha}^+$  and  $\hat{\alpha}^-$  in figure 9(a) demonstrate that indeed they originate from opposite half-planes.

After a first pinch point has been found, a continuation technique associated with an iterative procedure searching for zeros of  $\partial \hat{\Omega}^l / \partial \hat{\alpha}$  yields the absolute frequency  $\hat{\omega}_0$  and associated wavenumber  $\hat{\alpha}_0$  for nearby values of  $\hat{\beta}$  or of  $R$ ,  $\alpha$  and  $\beta$ . This iterative search requires only the computation of the mapping  $\hat{\alpha} \mapsto \hat{\omega}$ , which is numerically much faster (but still slow!) since the governing equations are of first order in time. Occasional spot checks using the (computationally more intensive) mapping  $\hat{\omega} \mapsto \hat{\alpha}$

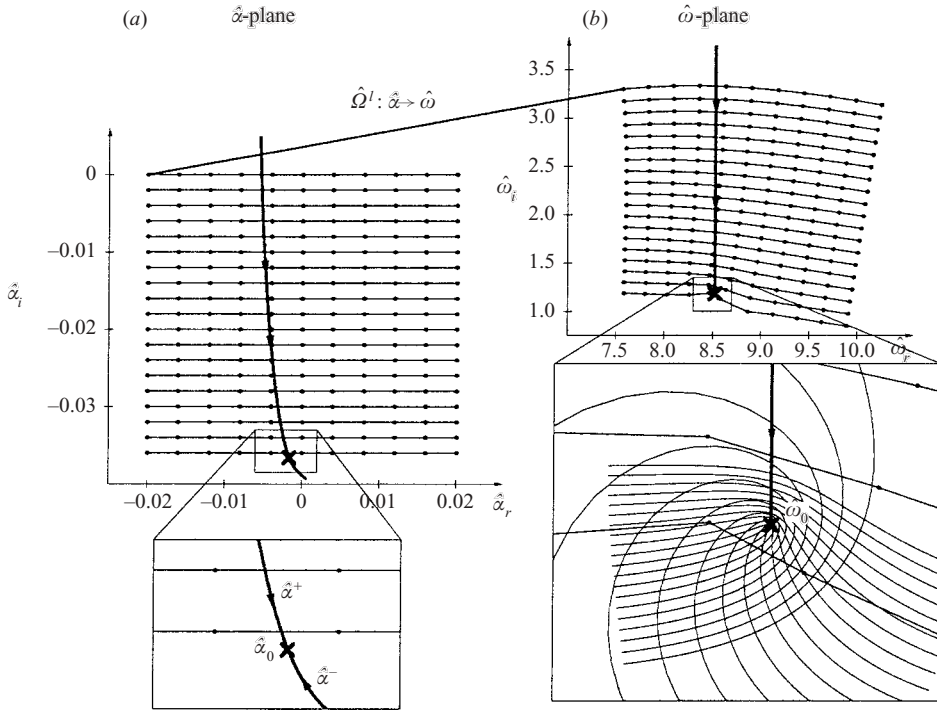


FIGURE 9. Mapping of the complex  $\hat{\alpha}$ -plane (a) onto the complex  $\hat{\omega}$ -plane (b) under the secondary dispersion relation  $\hat{\Omega}^I$  and identification of pinch point ( $\times$ ). Same primary wave as in figure 4, fixed secondary azimuthal wavenumber  $\beta = 20$ . Magnified portion of (b) shows cusp structure at  $\hat{\omega}_0$ . Vertical frequency path (thick line in b) is associated with two spatial branches  $\hat{\alpha}^+$  and  $\hat{\alpha}^-$  indicated by thick lines in (a). The two branches collide at absolute wavenumber  $\hat{\alpha}_0$  and originate from opposite half-planes for large values of  $\hat{\omega}_i$ .

are performed to ensure that the values of  $\hat{\alpha}_0$  and  $\hat{\omega}_0$  thus obtained are still associated with genuine pinch points.

The above analysis and result (7.8) are based on the nonlinear waves that are part of the self-sustained global solution and prevail for  $R = 510$ . As depicted in figure 9, the location of  $\hat{\omega}_0$  in the upper complex frequency plane then reveals that the *saturated crossflow vortices that are naturally selected near  $R^{ca}$  are absolutely unstable with respect to secondary perturbations*. This strong secondary absolute instability explains why the naturally selected spiral vortices (sketched in figure 7) are not observed experimentally: as soon as the primary nonlinear vortices are generated near  $R^{ca}$ , secondary perturbations develop *in situ* and are amplified by a factor of  $\exp(2\pi\hat{\omega}_{0,i}) \simeq 1500$  per disk rotation, and transition to turbulence immediately occurs.

The structure of the secondary eigenfunction associated with the pinch point of figure 9 is illustrated in figure 10 by its azimuthal velocity field  $\hat{v}^I(z, \phi)$ . Isocontours of (a) the velocity modulus  $|\hat{v}^I|$  and (b) its real part  $\hat{v}_r^I$  are shown over two wavelengths, superimposed on  $v^{nl}$ -levels of the primary nonlinear wave, from figure 4(ii)(a). The largest amplitude of the eigenfunction is seen to occur for  $\phi \simeq 3\pi/2$  and precisely correlates with the region where the primary wave displays strongly sheared velocity profiles, cf. figure 4(iii).



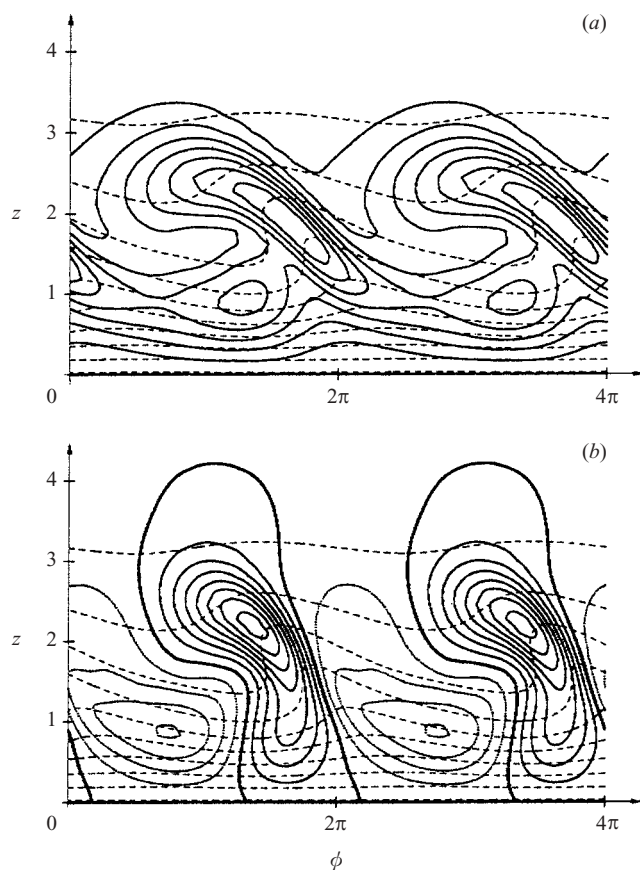


FIGURE 10. Structure of secondary eigenfunction associated with the pinch point of figure 9. Equispaced isolines of (a) modulus and (b) real part of azimuthal velocity component  $\hat{v}^l(z, \phi)$  superimposed on azimuthal isolines of primary nonlinear wave (thin dashed curves, cf. figure 4iia). Negative (zero) levels are shown by dotted (thick) curves.

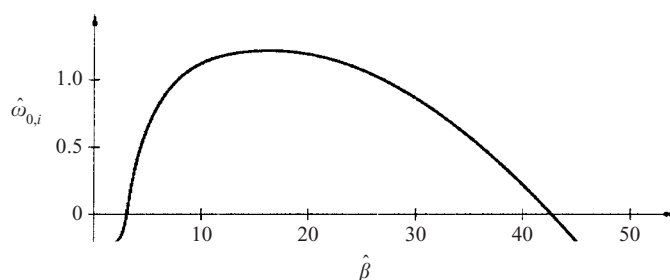


FIGURE 11. Secondary absolute growth rate  $\hat{\omega}_{0,i}(\hat{\beta})$  pertaining to primary crossflow vortices near onset of nonlinearity  $\alpha = 0.35$ ,  $\beta = 68$ ,  $\omega = 50.5$  and  $R = 510$ .

Figure 11 displays the variation of secondary absolute growth rate  $\hat{\omega}_{0,i}$  with mode number  $\hat{\beta}$ , computed for the same primary saturated vortices, and shows that secondary absolute instability prevails for a wide range of azimuthal mode numbers.

## 8. Conclusion

This study has demonstrated that the behaviour of the three-dimensional boundary layer produced by a rotating disk can be analysed in terms of an ‘elephant’ global mode: the self-sustained finite-amplitude fluctuations are produced at the inner boundary  $R^{ca}$  of the absolutely unstable domain. This boundary for onset of absolute instability acts as a source and generates outward-spiralling saturated primary crossflow vortices. Due to the slow radial development of the boundary layer, these wavetrains are governed locally by the associated nonlinear dispersion relation derived numerically from the local boundary layer velocity profiles considered as parallel. A secondary stability analysis has revealed that the primary saturated waves initiated at  $R^{ca}$  are already absolutely unstable with respect to secondary perturbations. The naturally selected structure is thus dynamically unstable and gives way to a disordered state. (Note that, strictly speaking, these results only pave the way towards transition: in order to fully document the route to turbulence one would need to establish that secondary instabilities themselves do not saturate.) In consequence, the rotating-disk flow follows the scenario first outlined by Huerre (1988), using model equations rather than based on the Navier–Stokes equations, that secondary absolute instability may occur prior to primary absolute instability.

It should be emphasized that, in the present configuration, transition to a turbulent flow is triggered by secondary absolute instability while the transition location itself is controlled by primary absolute instability. Indeed, primary nonlinear waves are a prerequisite for the development of secondary instability leading to transition. Since the secondary disturbances feed on the primary vortices, the turbulent régime cannot propagate inwards of  $R^{ca}$  and the central region remains unperturbed. As a result, the transition location from basic to turbulent flow precisely coincides with the onset of primary absolute instability. Thus the primary instability remains essential, even though the primary spiral waves are obliterated.

In the present findings, transition occurs via a primary state of azimuthal mode number  $\beta = 68$ , while the spiral structures that have been observed experimentally generally display fewer spiral arms, in the range 25–50. There is no inconsistency, however, since experimental measurements of  $\beta$  have only been done for crossflow vortices that are steady with respect to the disk: these steady structures are presumably produced by roughness elements on the disk surface, depend on the experimental conditions and differ in frequency and wavenumber from the naturally selected ones. Also, using a smooth disk, Lingwood (1996) has not observed any periodic vortices, only a sharp transition from the unperturbed boundary layer to turbulence. Hence it seems that the observation of primary vortices requires external forcing whereas transition is an intrinsic feature of the boundary layer. A further confirmation of this assertion is the wide scatter in the number of observed spiral arms, whereas transition always occurs at a well-defined location.

The present results emphasize the essential difference between rotating-disk and swept-wing boundary layers. The rotating-disk problem is primarily one-dimensional: its dynamics is organized in the radial direction while the azimuthal and wall-normal coordinates appear as eigendirections. In contrast, the swept-wing problem is genuinely two-dimensional which makes its investigation much harder both analytically and numerically. Azimuthal periodicity of the disk enables the intrinsic route to turbulence via primary and secondary absolute instabilities. The swept-wing flow undergoes primary and secondary convective instabilities which ‘initiate but do not instantly cause breakdown to turbulence’ (Koch 2002).

$N_z = 30$	$R^{ca}$	$\omega_0^{ca}$	$\alpha_0^{ca}$	$N_z = 40$	$R^{ca}$	$\omega_0^{ca}$	$\alpha_0^{ca}$
$a_\star = 1$	502.645	50.3471	0.21686 – 0.11819i	$a_\star = 1$	508.475	50.5285	0.21719 – 0.12281i
2	507.537	50.5043	0.21757 – 0.12208i	2	507.504	50.4952	0.21679 – 0.12188i
3	507.284	50.4885	0.21676 – 0.12166i	3	507.369	50.4926	0.21694 – 0.12177i
4	507.561	50.4974	0.21694 – 0.12184i	4	507.402	50.4933	0.21691 – 0.12180i
5	507.216	50.4876	0.21712 – 0.12190i	5	507.403	50.4934	0.21692 – 0.12180i
6	506.895	50.4822	0.21655 – 0.12202i	6	507.386	50.4929	0.21692 – 0.12180i
$N_z = 50$	$R^{ca}$	$\omega_0^{ca}$	$\alpha_0^{ca}$	$N_z = 60$	$R^{ca}$	$\omega_0^{ca}$	$\alpha_0^{ca}$
$a_\star = 1$	507.088	50.4836	0.21688 – 0.12148i	$a_\star = 1$	507.500	50.4961	0.21690 – 0.12191i
2	507.368	50.4925	0.21693 – 0.12177i	2	507.403	50.4934	0.21692 – 0.12181i
3	507.401	50.4934	0.21692 – 0.12180i	3	507.398	50.4932	0.21692 – 0.12180i
4	507.396	50.4932	0.21692 – 0.12180i	4	507.397	50.4932	0.21692 – 0.12180i
5	507.397	50.4932	0.21692 – 0.12180i	5	507.397	50.4932	0.21692 – 0.12180i
6	507.397	50.4932	0.21692 – 0.12180i	6	507.397	50.4932	0.21692 – 0.12180i

TABLE 1. Onset location  $R^{ca}$  of primary absolute instability at  $\beta = 68$  and corresponding absolute frequency  $\omega_0^{ca}$  and wavenumber  $\alpha_0^{ca}$ . Values computed with  $N_z = 30, 40, 50$  and 60 collocation points using transformation (4.3) with  $a_\star$  as given,  $b_\star = 0.6$  and  $c_\star = 0.5$ .

$N_z = 30$	$\alpha$	$E_1$	$E_2$	$E_3$	$E_4$	$E_5$	$N_z = 40$	$\alpha$	$E_1$	$E_2$	$E_3$	$E_4$	$E_5$
$N_h = 1$	0.33660	625.49					$N_h = 1$	0.33660	625.60				
2	0.34450	628.03	41.09				2	0.34450	628.09	41.12			
3	0.34607	622.24	37.63	3.88			3	0.34607	622.07	37.55	3.87		
4	0.34620	621.11	37.20	3.48	0.39		4	0.34616	621.10	37.13	3.45	0.38	
5	0.34620	620.97	37.13	3.45	0.35	0.04	5	0.34616	621.03	37.09	3.43	0.35	0.04
$N_z = 50$	$\alpha$	$E_1$	$E_2$	$E_3$	$E_4$	$E_5$	$N_z = 60$	$\alpha$	$E_1$	$E_2$	$E_3$	$E_4$	$E_5$
$N_h = 1$	0.33660	625.66					$N_h = 1$	0.33660	625.70				
2	0.34450	628.14	41.13				2	0.34450	628.16	41.14			
3	0.34607	622.11	37.56	3.87			3	0.34607	622.14	37.56	3.87		
4	0.34616	621.15	37.14	3.46	0.38		4	0.34616	621.17	37.14	3.46	0.38	
5	0.34616	621.08	37.10	3.43	0.35	0.04	5	0.34616	621.11	37.10	3.44	0.35	0.04

TABLE 2. Nonlinear wave at  $R = 510$  and  $\beta = 68$  with prescribed frequency  $\omega = 50.5$ . Values of radial wavenumber  $\alpha$  and harmonic energy content computed with  $N_z = 30, 40, 50, 60$  and  $N_h = 1, \dots, 5$ .

Suggestions and advice from Nigel Peake and Werner Koch are gratefully acknowledged. Special thanks go to Julian Scott for a careful reading of the manuscript and to Paul Metcalfe for so efficiently setting up the Linux boxes which made possible the numerical computations of the present paper.

## Appendix. Resolution tests

### A.1. Onset of primary absolute instability

Transition from primary linear convective to absolute instability first occurs for  $\beta = 68$ . Table 1 shows how the marginal location  $R^{ca}$ , the real marginal absolute frequency  $\omega_0^{ca}$  and the corresponding absolute wavenumber  $\alpha_0^{ca}$  depend on the number and distribution of axial collocation points.

$N_z = 30$	$\hat{N}_h = 1$	2	3	4	5
$N_h = 1$	8.8017 + 1.2062i	8.7483 + 1.1959i	8.7549 + 1.2132i	8.7556 + 1.2127i	8.7556 + 1.2127i
2	8.6422 + 1.0452i	8.5613 + 1.1728i	8.5409 + 1.2081i	8.5435 + 1.2110i	8.5437 + 1.2109i
3	8.5978 + 1.0262i	8.5197 + 1.1485i	8.5282 + 1.1858i	8.5266 + 1.1904i	8.5269 + 1.1907i
4	8.5931 + 1.0260i	8.5162 + 1.1470i	8.5254 + 1.1827i	8.5286 + 1.1882i	8.5285 + 1.1885i
5	8.5929 + 1.0263i	8.5163 + 1.1471i	8.5256 + 1.1827i	8.5289 + 1.1881i	8.5292 + 1.1886i
$N_z = 40$	$\hat{N}_h = 1$	2	3	4	5
$N_h = 1$	8.7915 + 1.1754i	8.7389 + 1.1699i	8.7457 + 1.1866i	8.7463 + 1.1862i	8.7463 + 1.1862i
2	8.6296 + 1.0153i	8.5492 + 1.1446i	8.5297 + 1.1792i	8.5324 + 1.1819i	8.5325 + 1.1818i
3	8.5859 + 0.9973i	8.5085 + 1.1208i	8.5182 + 1.1564i	8.5170 + 1.1609i	8.5173 + 1.1610i
4	8.5825 + 0.9975i	8.5062 + 1.1197i	8.5162 + 1.1539i	8.5200 + 1.1592i	8.5199 + 1.1595i
5	8.5825 + 0.9978i	8.5063 + 1.1198i	8.5165 + 1.1539i	8.5202 + 1.1592i	8.5207 + 1.1597i

TABLE 3. Secondary absolute frequency  $\hat{\omega}_0(\hat{\beta} = 20)$  pertaining to primary crossflow vortices near onset of nonlinearity  $\omega = 50.5$ ,  $\beta = 68$  and  $R = 510$ .

### A.2. Nonlinear wave near onset of primary absolute instability

Nonlinear waves prevailing at  $R = 510$  with  $\beta = 68$  and a prescribed frequency of  $\omega = 50.5$  have been computed for a range of resolutions. Table 2 shows how the corresponding radial wavenumber  $\alpha$  and the distribution of the energy content by harmonics depends on the number of collocation points and of harmonics used in the computation.

### A.3. Secondary absolute frequencies

Table 3 shows how the secondary absolute frequency  $\hat{\omega}_0$  for  $\hat{\beta} = 20$  depends on the number of primary  $N_h$  and secondary  $\hat{N}_h$  Fourier modes taken into account. The primary nonlinear wave at  $R = 510$ ,  $\beta = 68$  and  $\omega = 50.5$  is computed with  $N_z = 30$  or 40 collocation points remapped according to (4.3) using  $a_\star = 2$ ,  $b_\star = 0.6$  and  $c_\star = 0.5$ .

## REFERENCES

- BALACHANDAR, S., STREETT, C. L. & MALIK, M. R. 1992 Secondary instability in rotating-disk flow. *J. Fluid Mech.* **242**, 323–347.
- BALAKUMAR, P. & MALIK, M. R. 1990 Traveling disturbances in rotating-disk flow. *Theor. Comput. Fluid Dyn.* **2**, 125–137.
- BASSOM, A. P. & GAJJAR, J. S. B. 1988 Non-stationary cross-flow vortices in three-dimensional boundary-layer flows. *Proc. R. Soc. Lond. A* **417**, 179–212.
- BASSOM, A. P. & HALL, P. 1991 Concerning the interaction of non-stationary crossflow vortices in a three-dimensional boundary layer. *Q. J. Mech. Appl. Maths* **44**, 147–172.
- BATCHELOR, G. K. 1951 Note on a class of solutions for the Navier–Stokes equations representing steady rotationally-symmetric flow. *Q. J. Mech. Appl. Maths* **4**, 29–41.
- BATCHELOR, G. K. 1967 *An Introduction to Fluid Dynamics*. Cambridge: Cambridge University Press.
- BENDER, C. M. & ORSZAG, S. A. 1978 *Advanced Mathematical Methods for Scientists and Engineers*. McGraw-Hill.
- BERS, A. 1983 Space-time evolution of plasma instabilities—absolute and convective. In *Handbook of Plasma Physics* (ed. M. Rosenbluth & R. Sagdeev), pp. 451–517. North-Holland.
- BIPPES, H., MÜLLER, B. & WAGNER, M. 1991 Measurements and stability calculations of the disturbance growth in an unstable three-dimensional boundary layer. *Phys. Fluids A* **3**, 2371–2377.
- BRANCHER, P. & CHOMAZ, J.-M. 1997 Absolute and convective secondary instabilities in spatially periodic shear flows. *Phys. Rev. Lett.* **78**, 658–661.

- BREVDO, L. & BRIDGES, T. J. 1996 Absolute and convective instabilities of spatially periodic flows. *Phil. Trans. R. Soc. Lond. A* **354**, 1027–1064.
- BRIGGS, R. J. 1964 *Electron-stream Interaction with Plasmas*. MIT Press.
- CANUTO, C., HUSSAINI, M. J. & QUARTERONI, A. 1988 *Spectral Methods in Fluid Dynamics*. Springer.
- CEBECI, T., CHEN, H. H., ARNAL, D. & HUANG, T. T. 1991 Three-dimensional linear stability approach to transition on wings and bodies of revolution at incidence. *AIAA J.* **29**, 2077–2085.
- CEBECI, T. & STEWARTSON, K. 1980 On stability and transition in three-dimensional flows. *AIAA J.* **18**, 398–405.
- CHIN, D.-T. & LITT, M. 1972 An electrochemical study of flow instability on a rotating disk. *J. Fluid Mech.* **54**, 613–625.
- CHOMAZ, J.-M., COUAIRON, A. & JULIEN, S. 1999 Absolute and convective nature of the Eckhaus and zigzag instability with throughflow. *Phys. Fluids* **11**, 3369–3373.
- CHOMAZ, J.-M., HUERRE, P. & REDEKOPP, L. G. 1991 A frequency selection criterion in spatially developing flows. *Stud. Appl. Maths* **84**, 119–144.
- COUAIRON, A. & CHOMAZ, J.-M. 1996 Global instabilities in fully nonlinear systems. *Phys. Rev. Lett.* **77**, 4015–4018.
- COUAIRON, A. & CHOMAZ, J.-M. 1997a Absolute and convective instabilities, front velocities and global modes in nonlinear systems. *Physica D* **108**, 236–276.
- COUAIRON, A. & CHOMAZ, J.-M. 1997b Pattern selection in the presence of a cross flow. *Phys. Rev. Lett.* **79**, 2666–2669.
- COUAIRON, A. & CHOMAZ, J.-M. 1999a Fully nonlinear global modes in slowly varying flows. *Phys. Fluids* **11**, 3688–3703.
- COUAIRON, A. & CHOMAZ, J.-M. 1999b Primary and secondary nonlinear global instability. *Physica D* **132**, 428–456.
- DAVIES, C. & CARPENTER, P. W. 2003 Global behaviour corresponding to the absolute instability of the rotating-disk boundary layer. *J. Fluid Mech.* **486**, 287–329.
- DEE, G. & LANGER, J. S. 1983 Propagating pattern selection. *Phys. Rev. Lett.* **50**, 383–386.
- FALLER, A. 1991 Instability and transition of disturbed flow over a rotating disk. *J. Fluid Mech.* **230**, 245–269.
- FEDOROV, B. I., P LAVNIK, G. Z., PROKHOROV, I. V. & ZHUKHOVITSKH, L. G. 1976 Transitional flow conditions on a rotating disk. *J. Engng Phys.* **31**, 1448–1453.
- FISCHER, T. M. & DALLMANN, U. 1991 Primary and secondary stability analysis of three-dimensional boundary-layer flow. *Phys. Fluids A* **3**, 2378–2391.
- GAUTHIER, G., GONDRET, P. & RABAUD, M. 1999 Axisymmetric propagating vortices in the flow between a stationary and a rotating disk enclosed by a cylinder. *J. Fluid Mech.* **386**, 105–126.
- GREGORY, N., STUART, J. T. & WALKER, W. S. 1995 On the stability of three-dimensional boundary layers with application to the flow due to a rotating disk. *Phil. Trans. R. Soc. Lond. A* **248**, 155–199.
- HERBERT, T. 1988 Secondary instability of boundary layers. *Annu. Rev. Fluid Mech.* **20**, 487–526.
- HÖGBERG, M. & HENNINGSON, D. 1998 Secondary instability of cross-flow vortices in Falkner–Skan Cooke boundary layers. *J. Fluid Mech.* **368**, 339–357.
- HUERRE, P. 1988 On the absolute/convective nature of primary and secondary instabilities. In *Propagation in Systems far from Equilibrium* (ed. J. E. Wesfreid, H. R. Brand, P. Manneville, G. Albinet & N. Boccara), pp. 340–353. Springer.
- HUERRE, P. 2000 Open shear flow instabilities. In *Perspectives in Fluid Dynamics* (ed. G. K. Batchelor, H. K. Moffatt & M. G. Worster), pp. 159–229. Cambridge University Press.
- HUERRE, P. & MONKEWITZ, P. A. 1990 Local and global instabilities in spatially developing flows. *Annu. Rev. Fluid Mech.* **22**, 473–537.
- JANKE, E. & BALAKUMAR, P. 2000 On the secondary instability of three-dimensional boundary layers. *Theor. Comput. Fluid Dyn.* **14**, 167–194.
- JARRE, S., LE GAL, P. & CHAUVE, M. P. 1996a Experimental study of rotating disk instability, I. Natural flow. *Phys. Fluids* **8**, 496–508.
- JARRE, S., LE GAL, P. & CHAUVE, M. P. 1996b Experimental study of rotating disk flow instability, II. Forced flow. *Phys. Fluids* **8**, 2985–2994.
- VON KÁRMÁN, T. 1921 Über laminare und turbulente Reibung. *Z. Angew. Math. Mech.* **1**, 232–252.
- KELLER, H. B. 1977 Numerical solution of bifurcation and nonlinear eigenvalue problems. In *Applications of Bifurcation Theory* (ed. P. Rabinowitz), pp. 359–384. Academic.

- KOBAYASHI, R., KOHAMA, Y. & TAKAMADATE, C. 1980 Spiral vortices in boundary layer transition regime on a rotating disk. *Acta Mechanica* **35**, 71–82.
- KOCH, W. 1996 Nonlinear crossflow saturation in three-dimensional boundary layers. In *IUTAM Symp. on Nonlinear Instability and Transition in Three-Dimensional Boundary Layers* (ed. P. W. Duck & P. Hall), pp. 299–308. Kluwer.
- KOCH, W. 2002 On the spatio-temporal stability of primary and secondary crossflow vortices in a three-dimensional boundary layer. *J. Fluid Mech.* **456**, 85–111.
- KOCH, W., BERTOLOTI, F., STOLTE, A. & HEIN, S. 2000 Nonlinear equilibrium solutions in a three-dimensional boundary layer and their secondary instability. *J. Fluid Mech.* **406**, 131–174.
- KOHAMA, Y. 1984 Study on boundary layer transition of a rotating disk. *Acta Mechanica* **50**, 193–199.
- KUPFER, K., BERS, A. & RAM, A. K. 1987 The cusp map in the complex-frequency plane for absolute instabilities. *Phys. Fluids* **30**, 3075–3082.
- LE DIZÈS, S., HUERRE, P., CHOMAZ, J.-M. & MONKEWITZ, P. A. 1996 Linear global modes in spatially developing media. *Phil. Trans. R. Soc. Lond. A* **354**, 169–212.
- LE GAL, P., RAVOUX, J. F., FLORIANI, E. & DUDOK DE WIT, T. 2003 Recovering coefficients of the complex Ginzburg–Landau equation from experimental spatio-temporal data: two examples from hydrodynamics. *Physica D* **174**, 114–133.
- LIN, R. S. & REED, H. L. 1993 Effect of curvature on stationary cross-flow instability of a three-dimensional boundary layer. *AIAA J.* **31**, 1611–1617.
- LINGWOOD, R. J. 1995 Absolute instability of the boundary layer on a rotating disk. *J. Fluid Mech.* **299**, 17–33.
- LINGWOOD, R. J. 1996 An experimental study of absolute instability of the rotating-disk boundary-layer flow. *J. Fluid Mech.* **314**, 373–405.
- LINGWOOD, R. J. 1997a Absolute instability of the Ekman layer and related rotating flows. *J. Fluid Mech.* **331**, 405–428.
- LINGWOOD, R. J. 1997b On the impulse response for swept boundary-layer flows. *J. Fluid Mech.* **344**, 317–334.
- MALIK, M. R. 1986 The neutral curve for stationary disturbances in rotating-disk flow. *J. Fluid Mech.* **164**, 275–287.
- MALIK, M. R., LI, F. & CHANG, C.-L. 1994 Crossflow disturbances in three-dimensional boundary layers: nonlinear development, wave interaction and secondary instability. *J. Fluid Mech.* **268**, 1–36.
- MALIK, M. R., LI, F. & CHANG, C.-L. 1996 Nonlinear crossflow disturbances and secondary instabilities in swept-wing boundary layers. In *IUTAM Symp. on Nonlinear Instability and Transition in Three-Dimensional Boundary Layers* (ed. P. W. Duck & P. Hall), pp. 299–308. Kluwer.
- MALIK, M. R., LI, F., CHOUDHARI, M. M. & CHANG, C.-L. 1999 Secondary instability of crossflow vortices and swept-wing boundary-layer transition. *J. Fluid Mech.* **399**, 85–115.
- MALIK, M. R., WILKINSON, S. P. & ORSZAG, S. A. 1981 Instability and transition in rotating disk flow. *AIAA J.* **19**, 1131–1138.
- MONKEWITZ, P. A., HUERRE, P. & CHOMAZ, J.-M. 1993 Global linear stability analysis of weakly non-parallel shear flows. *J. Fluid Mech.* **251**, 1–20.
- PEAKE, N. & GARRETT, S. J. 2002 On the global linear stability of the boundary layer on rotating bodies. *J. Fluid Mech.* (submitted).
- PIER, B. 2002a Fully nonlinear waves and transition in the boundary layer over a rotating disk. In *Advances in Turbulence IX, Proc. 9th European Turbulence Conf.* (ed. I. Castro & P. Hancock), pp. 13–16. Barcelona: CIMNE.
- PIER, B. 2002b On the frequency selection of finite-amplitude vortex shedding in the cylinder wake. *J. Fluid Mech.* **458**, 407–417.
- PIER, B. & HUERRE, P. 1996 Fully nonlinear global modes in spatially developing media. *Physica D* **97**, 206–222.
- PIER, B. & HUERRE, P. 2001a Nonlinear self-sustained structures and fronts in spatially developing wake flows. *J. Fluid Mech.* **435**, 145–174.
- PIER, B. & HUERRE, P. 2001b Nonlinear synchronization in open flows. *J. Fluids Struct.* **15**, 471–480.
- PIER, B., HUERRE, P. & CHOMAZ, J.-M. 2001 Bifurcation to fully nonlinear synchronized structures in slowly varying media. *Physica D* **148**, 49–96.

- PIER, B., HUERRE, P., CHOMAZ, J.-M. & COUAIRON, A. 1998 Steep nonlinear global modes in spatially developing media. *Phys. Fluids* **10**, 2433–2435.
- REED, H. L. 1987 Wave interactions in swept-wing flows. *Phys. Fluids* **30**, 3419–3426.
- REED, H. L. & SARIC, W. S. 1989 Stability of three-dimensional boundary layers. *Annu. Rev. Fluid Mech.* **21**, 235–284.
- RYZHOV, O. S. & TERENT'EV, E. D. 1998 Streamwise absolute instability of a three-dimensional boundary layer at high Reynolds number. *J. Fluid Mech.* **373**, 111–153.
- SARIC, W. S., REED, H. L. & WHITE, E. B. 2003 Stability and transition of three-dimensional boundary layers. *Annu. Rev. Fluid Mech.* **35**, 413–440.
- SCHMID, P. J. & HENNINGSON, D. S. 2000 *Stability and Transition in Shear Flows*. Springer.
- SCHOUVEILER, L., LE GAL, P. & CHAUVE, M. P. 2001 Instabilities of the flow between a rotating and a stationary disk. *J. Fluid Mech.* **443**, 329–350.
- SERRE, E., CRESPO DEL ARCO, E. & BONToux, P. 2001a Annular and spiral patterns in flows between rotating and stationary disks. *J. Fluid Mech.* **434**, 65–100.
- SERRE, E., HUGUES, S., CRESPO DEL ARCO, E., RANDRIAMAMPANINA, A. & BONToux, P. 2001b Axisymmetric and three-dimensional instabilities in an Ekman boundary layer flow. *Intl. J. Heat Fluid Flow* **22**, 82–93.
- TAYLOR, M. J. & PEAKE, N. 1998 The long-time behaviour of incompressible swept-wing boundary layers subject to impulsive forcing. *J. Fluid Mech.* **355**, 359–381.
- THEODORSEN, T. & REGIER, A. 1944 Experiments on drag of revolving disks, cylinders, and streamline rods at high speeds. *Tech. Rep.* 793. NACA.
- WILKINSON, S. P. & MALIK, M. R. 1985 Stability experiments in the flow over a rotating disk. *AIAA J.* **23**, 588–595.
- ZANDBERGEN, P. J. & DIJKSTRA, D. 1987 Von Kármán swirling flows. *Annu. Rev. Fluid Mech.* **19**, 465–491.